National Library of Canada

Acquisitions and Bibliographic Services Branch

395 Wellington Street
Ottawa, Ontario
K1A 0N4

Bibliothèque nationale du Canada

Direction des acquisitions et des services bibliographiques

395, rue Wellington
Ottawa (Ontario)
K1A 0N4

Your file *Votre référence*

Our file *Notre référence*

NOTICE

The quality of this microform is heavily dependent upon the quality of the original thesis submitted for microfilming. Every effort has been made to ensure the highest quality of reproduction possible.

If pages are missing, contact the university which granted the degree.

Some pages may have indistinct print especially if the original pages were typed with a poor typewriter ribbon or if the university sent us an inferior photocopy.

Reproduction in full or in part of this microform is governed by the Canadian Copyright Act, R.S.C. 1970, c. C-30, and subsequent amendments.

AVIS

La qualité de cette microforme dépend grandement de la qualité de la thèse soumise au microfilmage. Nous avons tout fait pour assurer une qualité supérieure de reproduction.

S'il manque des pages, veuillez communiquer avec l'université qui a conféré le grade.

La qualité d'impression de certaines pages peut laisser à désirer, surtout si les pages originales ont été dactylographiées à l'aide d'un ruban usé ou si l'université nous a fait parvenir une photocopie de qualité inférieure.

La reproduction, même partielle, de cette microforme est soumise à la Loi canadienne sur le droit d'auteur, SRC 1970, c. C-30, et ses amendements subséquents.

Canada

HIGH RESOLUTION FOURIER TRANSFORM PHOTOLUMINESCENCE SPECTROSCOPY OF BOUND EXCITONS IN SILICON

BY
DARLENE BRAKE
B.Sc. MEMORIAL UNIVERSITY OF NEWFOUNDLAND 1989

THIS THESIS IS SUBMITTED IN PARTIAL FULFILLMENT OF THE REQUIREMENTS FOR THE DEGREE OF MASTER OF SCIENCE IN THE DEPARTMENT OF PHYSICS

© DARLENE BRAKE
SIMON FRASER UNIVERSITY
JUNE 1992

ISBN 0-315-83746-2

APPROVAL

NAME: DARLENE BRAKE

DEGREE: MASTER OF SCIENCE

THESIS TITLE: HIGH RESOLUTION FOURIER TRANSFORM PHOTOLUMINESCENCE SPECTROSCOPY OF BOUND EXCITONS IN SILICON

EXAMINING COMMITTEE:

CHAIRMAN: DR. S. Cygax

DR. M.L.W. THEWALT
Senior Supervisor

DR. A.E. CURZON

DR. J.C. IRWIN

DR. R.F. FRINDT
External Examiner
Department of Physics
Simon Fraser University

DATE APPROVED: June 12, 1992

PARTIAL COPYRIGHT LICENSE

I hereby grant to Simon Fraser University the right to lend my thesis, project or extended essay (the title of which is shown below) to users of the Simon Fraser University Library, and to make partial or single copies only for such users or in response to a request from the library of any other university, or other educational institution, on its own behalf or for one of its users. I further agree that permission for multiple copying of this work for scholarly purposes may be granted by me or the Dean of Graduate Studies. It is understood that copying or publication of this work for financial gain shall not be allowed without my written permission.

Title of Thesis/Project/Extended Essay

High Resolution Fourier Transform Photoluminescence Spectroscopy of Bound Excitons in Silicon

Author:

(signature)

Darlene M Brake

(name)

July 29/92

(date)

ABSTRACT

Fourier transform photoluminescence spectroscopy using a Michelson interferometer has been applied to the study of donor and acceptor bound exciton complexes in silicon. This technique can be used to collect very high resolution spectra with a high signal to noise ratio, and has thus allowed us to probe the fine structure of the bound exciton spectral lines more thoroughly than previous researchers. Ultra high resolution spectra of bound exciton transitions in silicon, containing the donors phosphorous and arsenic, and the acceptors aluminum, gallium, indium, and boron, have been collected. While the lack of structure in the donor bound exciton spectra can be explained in the framework of the existing model of bound excitons, the additional fine structure seen in the acceptor bound exciton spectra can not be reconciled with it. The effect of uniaxial stress on the spectrum of the boron bound exciton has been investigated in an attempt to determine the interactions responsible for the zero stress fine structure. The results of this investigation have been used to test a new, recently proposed, model of the boron bound exciton.

ACKNOWLEDGEMENT

I would like to thank the SFU physics department, and in particular Dr. M.L.W. Thewalt and the "Thewalt lab group", for creating an exciting and productive research environment. Special thanks to Dr. Thewalt for suggesting this project, and to Dr. V.A. Karasyuk for his helpful discussions. The generous financial support from the Natural Sciences and Engineering Council of Canada, Simon Fraser University, and Dr.Thewalt was also greatly appreciated.

I am indebted to both Oliver and Sharon for all their support and encouragement.

Table of Contents

TABLE OF CONTENTS CONT'D

List of Figures

List of Figures Cont'd

List of Tables

Chapter One

Excitons and Photoluminescence in Silicon

1.1 Introduction

Since their discovery in 1960 [60H], the study of bound exciton complexes associated with donor and acceptor impurities in silicon has been of interest to the scientific community. Aside from the technologically important aspect of characterizing impurities in silicon, the study of impurity bound excitons is of some fundamental significance.

In early studies, the bound exciton photoluminescence spectral line was observed as an unsplit line lying at an energy characteristic of the impurity to which the exciton was bound [60H]. As technology improved, conventional dispersive spectrometers were able to resolve fine structure on some of the acceptor bound exciton lines [67D]. In 1977 the Kirczenow Shell Model for bound excitons, which was able to completely explain all the structure seen up to that time, was proposed [77K] [77T1] [77T2]. Since then however, advancements in spectroscopic technique have shown additional fine structure in the luminescence associated with the shallow acceptor bound excitons [88G]. In this thesis, Fourier transform spectroscopy using a Michelson interferometer has been applied to the study of shallow donor and acceptor bound exciton complexes. The results presented here represent the highest

resolution spectra of photoluminescence from silicon doped with acceptors aluminum, gallium, indium, and boron and donors phosphorous and arsenic collected to date.

This first chapter discusses excitons and photoluminescence in silicon. The discussion includes the behavior of shallow impurities and impurity bound excitons in silicon, plus an introduction to the Shell model and recent modifications to it. The experimental apparatus and techniques used to perform the experiments are described in chapter two. Chapter three presents high resolution spectra of the donor and acceptor bound exciton luminescence at zero stress, and interprets the structure in terms of the conventional shell model. The last chapter discusses the results of a study of the boron bound exciton luminescence under uniaxial stress.

1.2 SILICON

Silicon crystallizes in a diamond structure. It has an fcc Bravais lattice with a two atom basis, with atoms located at (000) and $a/4(111)$, and a lattice constant a = 5.43 Å [89L]. Pure silicon exhibits full cubic symmetry and belongs to the O_h point group. Figs. 1.1(a)-(c) show the diamond structure, the unit cell of its Bravais lattice, and its first Brillouin zone [76A]. A compilation of some physical and electronic properties of silicon [89L] is presented in Table 1.

Fig. 1.2(a) is the band diagram for silicon which shows the electron

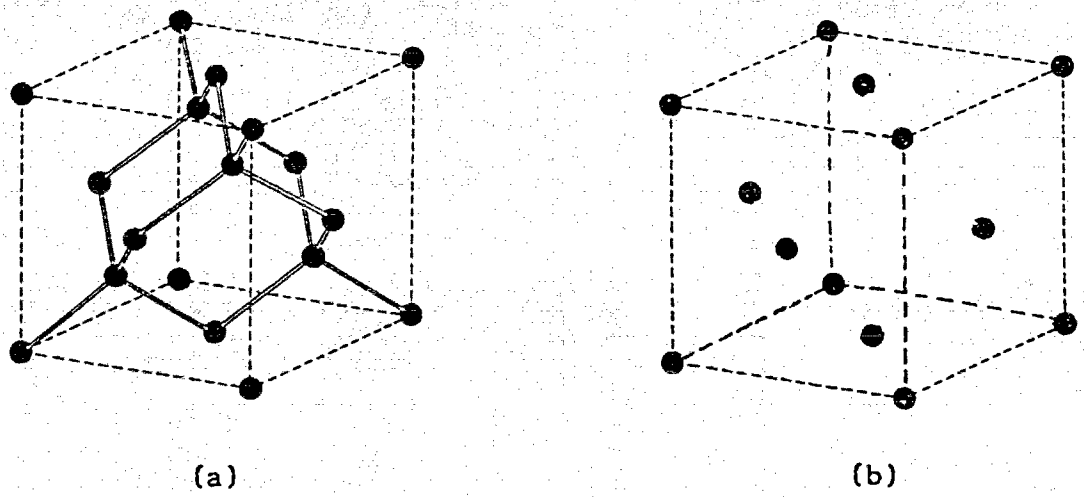

(a) (b)

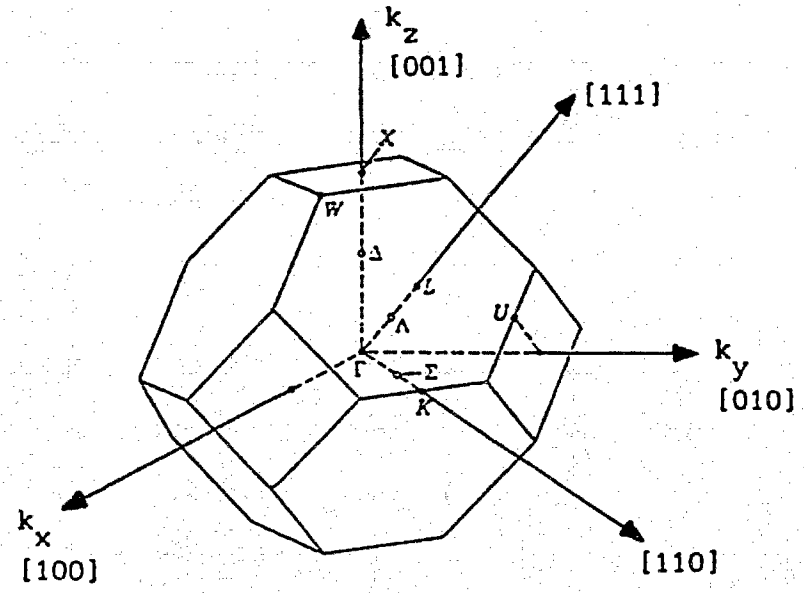

(c)

Fig. 1.1 (a) Diamond crystal structure. (b) Fcc Bravais lattice. (c) First Brillouin zone of the fcc lattice.

TABLE 1

crystal structure	face centered cubic
lattice constant (Å)	5.43
indirect band gap at 4.2 K (eV)	1.170
static dielectric constant, ε_r, at 4.2 K	12.1
Ionization Energy (eV)	
† Si:B	0.045
† Si:Al	0.069
† Si:Ga	0.071
† Si:In	0.155
† Si:Tl	0.246
‡ Si:P	0.045
‡ Si:As	0.054
‡ Si:Bi	0.071

† relative to the valence band edge

‡ relative to the conduction band edge

Reference [89L]

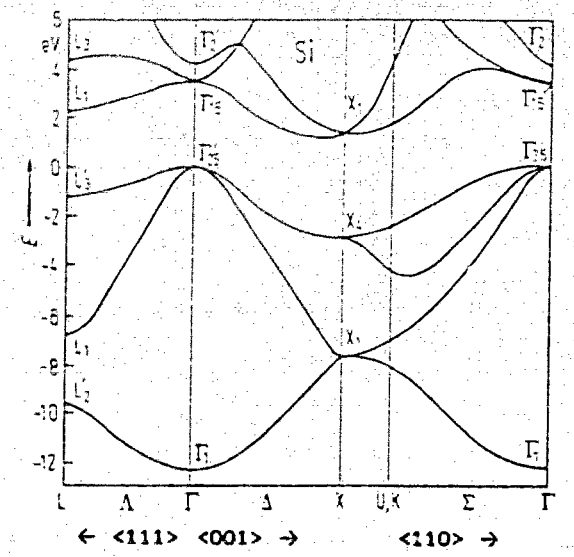

(a)

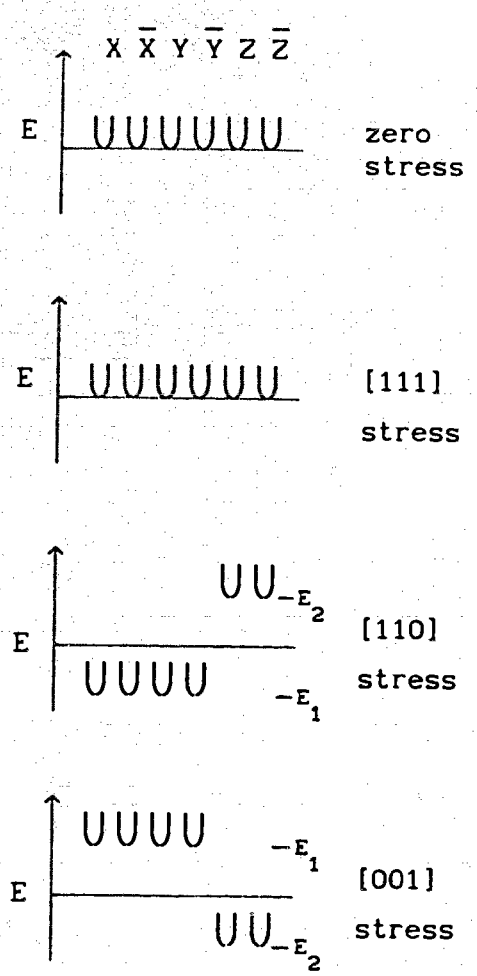

(b)

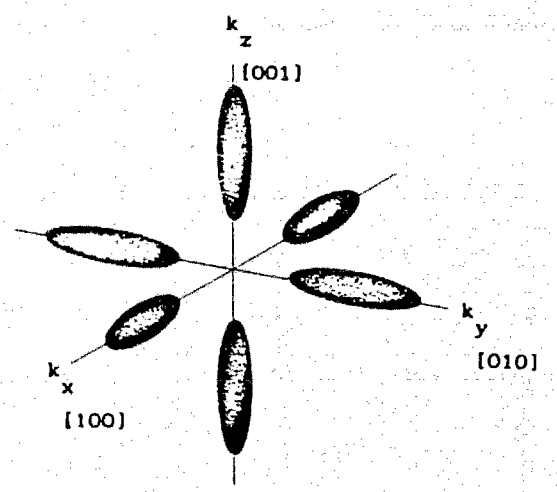

(c)

Fig.1.2. (a) Band structure of silicon [89L]. (b) Constant energy surface in of the conduction band edge [76A]. (c) Behavior of the six conduction band minima under compressive uniaxial stress

energy levels as a function of various directions in **k**-space, including <111>, <001> and <110>. A minimum of the conduction band occurs along the <001> directions at 85 % of the way to the zone boundary [89L]. The constant energy surface near the bottom of this conduction band valley is an ellipsoid of revolution which has its long axis along the <001> direction. The cubic symmetry of the lattice implies that a conduction band minimum occurs along *each* of the six equivalent [100] directions and thus the constant energy surface in **k**-space will consists of six equivalent ellipsoids, as depicted in Fig.1.2(b). For convenient reference, the minima along [100], $[\bar{1}00]$, [010], $[0\bar{1}0]$, [001], and $[00\bar{1}]$ are labelled X, $\bar{X}$, Y, $\bar{Y}$, Z, and $\bar{Z}$ valleys respectively.

The valence band maximum occurs at $\mathbf{k} = 0$ in the first Brillouin zone and is two fold degenerate (four-fold counting spin). The constant energy surface near the top of the valence band is thus somewhat complicated and consists of two concentric warped spheres [82S].

We define uniaxial stress as a force applied along a single crystallographic axis, and it will hereafter be assumed that this force is compressive. Application of stress can lift the degeneracies of the valence and conduction bands [81R]. The two-fold degeneracy of the valence band will be lifted by stress along any direction, splitting it into two bands. In the spectroscopic notation, these bands are labelled as $m_j = \pm 3/2$ and $m_j = \pm 1/2$, with the latter being the lowest in energy. The effect of stress on the conduction band degeneracy is illustrated in Fig.1.2(c), which sketches the behavior of the six minima under uniaxial stress. When stress is applied along <111>, the components of stress in all <001> directions are equivalent and there will be no change in the

energy of the valleys relative to each other, i.e the six-fold degeneracy remains. For stress applied along <110> or <001>, the bands will shift so that four band minima are at energy E_1 and two are at energy E_2 from the zero-stress equilibrium energy position, E_0. In the case of <110> stress, $E_1 < E_0 < E_2$ and in the case of <001> stress $E_1 > E_0 > E_2$ [81R].

1.3 SHALLOW IMPURITIES IN SEMICONDUCTORS

Each atom in a perfect silicon lattice forms four covalent bonds - one with each of it's four nearest neighbors. When an impurity is introduced, it takes the place of a silicon atom in the lattice, and the symmetry in the vicinity of the impurity is reduced from cubic O_h symmetry to tetrahedral T_d symmetry. Four electrons go towards forming the bonds and in trivalent (group III) acceptors, this results in a hole being liberated while in the pentavalent (group V) donors it results in a liberated electron. The acceptor can now be visualized as a *negatively* charged ion core and a liberated *hole* bound together by a Coulomb attraction. Similarly, the donor can be seen as a *positively* charged core and a liberated *electron*. The charge of the ion core polarizes the host medium which leads to dielectric screening; this reduces the Coulomb potential at the position of the hole (electron) by a factor $1/\varepsilon_r$ of its free space value, where ε_r is the dielectric constant (or relative permittivity) of the crystal. The ionization energy is defined in this context as the energy that binds the liberated

hole or electron to the ion core.

In this thesis, two classes of impurity states are discussed, namely *donor* states and *acceptor* states. A shallow donor state is characterized by an energy slightly below the conduction band, and a shallow acceptor state by an energy slightly above the valence band. The position of the impurity ground state relative to its associated band edge determines its ionization energy, which for typical shallow impurities in silicon are of the order of 50 meV [89L].

In free space, the excess hole or electron would move with a mass m. In a solid, however, the periodic potential influences the motion and the hole or electron travels instead with a mass m^* known as the effective mass, which depends on the direction the hole or electron moves in. The effective masses essentially reflect the curvature of the valence and conduction band edges and thus characterize the behavior of holes and electrons, since these will be found primarily in levels near the band edges. In silicon the effective mass is anisotropic and thus the effective mass tensor does not simply reduce to a scalar value m^*. For example, the electron effective mass is characterized by a transverse and a longitudinal mass which originate from the distinct curvature of the constant energy surface.

Both donor and acceptor states are analogous in a general way. However, donor state wavefunctions are made up primarily of wavefunctions chosen from near the conduction band edge whereas acceptor state wavefunctions are composed mainly of wavefunctions near the valence band edge. Donor and acceptor impurities in semiconductors are often modeled as solid state analogs of the hydrogen atom. Effective

mass theory is used to describe the electronic levels of the single hole or electron associated with the impurity ion in the crystal lattice. This theory was originally formulated by Kohn and Luttinger [55K] and has since then been reviewed and applied by a number of researchers, among them Bassani and Parravicini [75B], Ramdas and Rodrigues [81R], and Lannoo and Bourgoin [81L].

The most simple application of effective mass theory is to a donor state in a lattice having a single non-degenerate conduction band minimum. Applying effective mass theory to donors in silicon is more complicated due to silicon's six conduction band minima, but it is still relatively straightforward once the anisotropic effective mass tensor and the presence of multiple extrema are taken into account. Acceptors in silicon are more challenging, since their description involves hole states from the top of the valence band. Unlike the conduction band, the anisotropy of the valence band can not be simply described by a longitudinal and transverse effective mass since the curvature of the band edge is more complicated [82S] [57K].

The Schrödinger equation for the electron or hole associated with an impurity ion in a silicon lattice is written as

$$(H_0 + V(r))\, \psi_n(r) = E_n\, \psi_n(r) \qquad \text{eqn. (1.1)}$$

where H_0 is the perfect crystal Hamiltonian, $V(r)$ is the perturbation introduced by the impurity, and E_n is the bound state energy. The bound state wavefunctions $\psi_n(r)$ can be expressed as

$$\psi_n(\mathbf{r}) = \phi_n(\mathbf{r})\ \chi_k(\mathbf{r}) \qquad \text{eqn. (1.2)}$$

where $\chi_k(\mathbf{r})$ is the Bloch wave at the minimum located at wavevector $\mathbf{k}$, and the $\phi_n(\mathbf{r})$ are slowly varying envelope functions which, in the simplest case of one non-degenerate extremum and an isotropic effective mass m^*, satisfy the effective mass equation

$$\left[-\frac{\hbar^2}{2m^*}\nabla^2 + V(\mathbf{r}) \right] \phi_n(\mathbf{r}) = \mathcal{E}_n\ \phi_n(\mathbf{r}) \qquad \text{eqn. (1.3)}$$

The potential $V(\mathbf{r})$ can be approximated by

$$V(\mathbf{r}) = V(r) = \mp \frac{e^2}{4\pi\varepsilon_o \varepsilon_r r} \qquad \text{eqn. (1.4)}$$

where ε_r is the dielectric constant of the crystal, e is the electronic charge and r is the distance of the electron (- sign) or hole (+ sign) from the center of the impurity nucleus which is chosen as the coordinate origin. Eqn. (1.3) becomes an equation like the one that describes the hydrogen atom, and has solutions

$$\mathcal{E}_n = \pm \frac{m^* e^4}{(4\pi\varepsilon_o)^2 2\hbar^2 \varepsilon_r^2 n^2} \qquad \text{eqn. (1.5)}$$

which are the energies of the bound states relative to the band edge,

i.e $\mathcal{E}_n$ above the valence band maximum (acceptors) or below the conduction band minimum (donors). This solution predicts that all donors and all acceptors will have the same ionization energy, which is not experimentally observed. Rather, as shown in Table 1, the group III acceptors have ionization energies ranging from 45 meV to 246 meV and the group V donors from 45 meV to 71 meV. This discrepancy arises because so far the anisotropy of the effective mass, the presence of more than one conduction band minimum, and any deviations from a simple Coulombic potential have been neglected.

Consideration of the anisotropy of the effective mass, and the degeneracy of the conduction band minima alone leads to a separate acceptor ionization energy and a separate donor ionization energy. If the band anisotropy in silicon is considered, the effective mass equation, eqn. (1.3), becomes

$$\left[\frac{\hbar^2}{2m_l} \frac{\partial^2}{\partial z^2} - \frac{\hbar^2}{2m_t} \left(\frac{\partial^2}{\partial x^2} + \frac{\partial^2}{\partial y^2} \right) + V(r) \right] \phi_n(r) = \mathcal{E}_n \phi_n(r) \qquad \text{eqn. (1.6)}$$

for electron states. For hole states, using the same potential with opposite sign, the effective mass equation has the form

$$\sum_{j'=1}^{6} D^{\alpha\beta}_{jj'} \left(\frac{1}{i} \frac{\partial}{\partial x^\alpha} \right) \left(\frac{1}{i} \frac{\partial}{\partial x^\beta} \right) \phi_{j'}(r) - \lambda \xi_j \phi_j(r) + V(r) \phi_j(r) = \mathcal{E} \phi_j(r)$$

$$j = 1, \ldots, 6.$$

eqn. (1.7)

where the $D^{\alpha\beta}_{jj'}$ are numerical constants characteristic of silicon, λ is the energy difference between the top valence band and the spin-orbit split band below it, and $\xi_j = 0$ for $j = 1,2,3,4$ and $\xi_j = 1$ for $j = 5,6$. There are no analytical solutions of these equations, but calculations [55K] [75B] give bound state energies.

For donors, we consider the six equivalent minima of the conduction band (X, $\bar{X}$, Y, $\bar{Y}$, Z, $\bar{Z}$) and find that the solution of eqn. (1.6) has six equivalent electron wavefunctions $\phi^{(j)}_n(\mathbf{r})$, j=1,..,6, which are degenerate in energy. Using eqn. (1.2), we obtain for the lowest energy state 1s-like wavefunctions $\psi^{(j)}_{1s}(\mathbf{r})$. However this degeneracy is not permitted by the symmetry of the lattice, which has been reduced from full O_h by the presence of the impurity. These states must therefore "valley-orbit" split into states which belong to irreducible representations of the new symmetry group T_d. It has been shown [55K] [75B] that the ground state decomposes into the irreducible representations Γ_1, Γ_3, and Γ_5 which are one-, two-, and three-fold degenerate (two-, four-, and six-fold counting spin). The correct symmetry is obtained by a linear combination of the 1s-like wavefunctions $\psi^{(j)}_{1s}(\mathbf{r})$

$$\Psi_i(\mathbf{r}) = \sum_{j=i}^{6} \alpha^{(j)}_i \psi^{(j)}_{1s}(\mathbf{r}) \qquad i = 1,\ldots,6. \qquad \text{eqn. (1.8)}$$

where $\alpha^{(j)}_i$ are components of a matrix with row index i and column index j. The corresponding row vectors are

$$\left.\begin{aligned} \alpha_1^{(j)} &= \frac{1}{\sqrt{6}}\,(1,1,1,1,1,1) \end{aligned}\right\} \quad \Gamma_1$$

$$\left.\begin{aligned} \alpha_2^{(j)} &= \frac{1}{\sqrt{12}}\,(-1,-1,-1,-1,2,2) \\ \alpha_3^{(j)} &= \frac{1}{2}\,(1,1,-1,-1,0,0) \end{aligned}\right\} \quad \Gamma_3$$

$$\left.\begin{aligned} \alpha_4^{(j)} &= \frac{1}{\sqrt{2}}\,(1,-1,0,0,0,0) \\ \alpha_5^{(j)} &= \frac{1}{\sqrt{2}}\,(0,0,1,-1,0,0) \\ \alpha_6^{(j)} &= \frac{1}{\sqrt{2}}\,(0,0,0,0,1,-1) \end{aligned}\right\} \quad \Gamma_5$$

For acceptors, the above considerations do not apply, since we only need to consider a single band extremum, namely the valence band maximum at $\mathbf{k}=0$. The solutions of the acceptor effective mass equation (eqn. (1.7)) have Γ_8 symmetry, and since Γ_8 is an irreducible representation of T_d, when the symmetry of the crystal is reduced from O_h to T_d there will be no splitting of the acceptor ground state.

The range of both donor and acceptor ionization energies can be accounted for in these calculations by considering impurity-specific deviations of $V(\mathbf{r})$ from a simple Coulomb potential. One of the main assumptions in arriving at eqn. (1.5) was that the potential $V(r)$ varied slowly compared with the crystal potential included in H_0. This led to the possibility of writing the solution of the Schrödinger equation, eqn. (1.1), as the product of two wavefunctions, each solving a

Schrödinger equation (one involving the potential V(r), the other just the crystal potential yielding the Bloch wavefunction).

However, in a region where the above assumption is not true, some corrections have to be made. This is the case in the vicinity of the impurity, where the Coulomb potential varies rapidly (i.e. as 1/r for $r \rightarrow 0$). The associated correction term is therefore known as the "central cell correction" and is impurity specific. It becomes important when we consider the 1s-like wavefunctions associated with the ground states of the electron (in the donor case) or the hole (in the acceptor case), since those wavefunctions have maximum probability density at r=0. For higher energy states, whose wavefunctions are p-like and thus have zero amplitude at r=0, we expect the central cell correction to be negligible.

Thus at zero stress, we expect a non-split, two-fold degenerate (not counting spin) acceptor ground state, and a donor state which is valley-orbit-split into a non-degenerate Γ_1 state, a two-fold degenerate Γ_3 state, and a three-fold degenerate Γ_5 state. The energies of these states depend on the impurity being considered.

1.4 EXCITONS AND PHOTOLUMINESCENCE

1.4.1 Free excitons

An exciton is an electron-hole pair bound by an electrostatic interaction. It is typically formed when a photon with above band-gap energy excites an electron from the valence band to the conduction band,

leaving a hole behind. Excitons have lifetimes of nanoseconds to milliseconds, after which the electron and hole recombine, emitting a photon of characteristic energy.

The spatial extent of the exciton relative to the atomic spacing divides their discussion into two regimes [81K1]. In the first, the electron and hole constituting the exciton are tightly bound to each other and the exciton radius is of the order of the lattice spacing. These excitons are found primarily in ionic crystals and are known as Frenkel excitons. In the second regime, the constituents are loosely bound and the exciton radius is much larger than the lattice spacing. These are known as Wannier-Mott excitons and are most common in covalent crystals such as the elemental semiconductor silicon.

The analogy between the exciton and the hydrogen atom is often drawn as it was done for neutral impurities in the previous section. The electron and hole are treated as two charged particles with effective masses m_e^* and m_h^* that correspond to the curvature of the local band extrema. The Coulomb potential between them can be written as

$$U(r) = - \frac{e^2}{4\pi\varepsilon_o \varepsilon_r r} \qquad \text{eqn. (1.9)}$$

where e is the electronic charge, ε_r is the dielectric constant (relative permittivity) of the crystal and r is the particle separation. The energy of the bound states relative to that of a free electron and a free hole is

$$E_{n(FE)} = E_g - E_b^n$$

$$E_b^n = \frac{\mu e^4}{(4\pi\varepsilon_o)^2 2\hbar^2 \varepsilon_r^2 n^2} \qquad n = 1,2,3,\ldots \qquad \text{eqn. (1.10)}$$

where E_g is the band gap energy, E_b^n the exciton binding energy, and $\mu \equiv (1/m_e^* + 1/m_h^*)^{-1}$ is the reduced mass. Choosing typical values for silicon - μ equal to $0.12m_o$ (m_o being the free space electron mass) [77R] and ε_r equal to 12.1 in eqn.(1.10) yield a "Rydberg" , E_b^1, for the free exciton of about 11 meV, and a "Bohr radius", a_o, which is approximately 53 Å. This can be contrasted with the hydrogen atom Rydberg of 13.6 eV and Bohr radius of 0.51 Å. These excitonic processes must thus be studied in cryogenic environments since the binding energies are small compared to kT at room temperature.

1.4.2 Bound excitons

A free exciton travelling in a crystal can become localized at an impurity site, thus lowering it's energy by an amount E_L, the localization energy. This complex is called a bound exciton (BE) and can be viewed as an analogue of the hydrogen *molecule* in keeping with the previous treatment of the impurity and free exciton bound states. The energy of the bound exciton, E_{BE}, is given as

$$E_{BE} = E_{FE} - E_L \qquad \text{eqn. (1.11)}$$

where E_{FE} is the energy of the free exciton. E_L (and thus E_{BE}) is impurity specific, due mainly to the central cell correction mentioned earlier. The existence of bound excitons was first proposed by Lampert [58L] and later observed experimentally by Haynes [60H] who noted sharp luminescence lines at energies lower than the free exciton energy. These lines correspond to electron-hole recombination and the observed luminescence lines lie at energy E_{BE}.

1.4.3 Bound Multiexciton Complexes

It is possible for more than one exciton to become bound to an impurity site to form a bound multiexciton complex (BMEC). In 1970, a series of luminescence lines at energies below those of the bound exciton were observed [70K1, 70K2, 70P] and it was proposed that they originated from electron-hole recombination in complexes made up of more than one exciton bound to a neutral impurity. The proposed modeling scheme was heatedly debated for years [73S] [74K] [76S] [76M] [76D] [77T]. Finally, in 1977 the debate was settled with the development of the Kirczenow Shell Model for bound excitons and bound multiexciton complexes [77K] which was able to explain all the experimental results known at that time [77T1] [77T2].

1.4.4 Photoluminescence

The photoluminescence (PL) observed in this study is due to the

recombination of electrons and holes in excitonic complexes. When an electron-hole pair recombines, a photon characteristic of the complex is emitted. Since silicon is an indirect gap semiconductor, a **k**-vector conserving process, in addition to the absorption or emission of a photon, is typically involved when electron-hole pairs are created or recombined. Usually a phonon fulfills the conservation of **k**-vector requirements and the observed excitonic transitions are shifted in energy by an amount corresponding to the phonon energy. However, in doped silicon, it is possible to see no-phonon as well as phonon-assisted transitions since spatial localization of an exciton to an impurity site in real space leads to a greater diffuseness of the electron and hole wavefunctions in k-space. This allows greater overlap of electron and hole wavefunctions in k-space and thus permits electron-hole transitions which conserve k-vector. The intensity of no-phonon transitions will therefore increase with increasing exciton localization energy (greater localization in real space implies more diffuseness in **k**-space). Phonon assisted transitions will in general be broader than no-phonon transitions due to the dispersion in the phonon spectrum. This broadening mechanism is known as phonon-broadening and is discussed in ref. [63K].

1.5 THE SHELL MODEL

The Kirczenow shell model was developed to describe bound excitons and bound multiexciton complexes. This discussion will focus primarily

on the aspects of the model which pertain to acceptor and donor bound excitons and neglect the aspects of the model which deal with bound multiexciton complexes. A thorough review of this model and its numerous applications can be found in refs. [77K] [77T] [79T] and [82T].

In the general shell model, the impurity bound exciton or bound multiexciton complex is seen as an ionized core plus a collection of electrons and holes, with all the electrons and all the holes being treated on equal footing. The wavefunction of the electrons and the wavefunction of the holes are the properly antisymmetrized products of the corresponding single particle wavefunctions, each of which is characterized by its transformation properties under the T_d point group. The "shell-ness" of this model lies in the way the single particle states fill up with electrons and holes. All transitions are assumed to be single-electron into single-hole transitions, which is to say that one electron-hole pair recombines without affecting the other single particle states. A collective wave function formed by a product of single particle irreducible T_d representations will in general be reducible. It is thus necessary to examine the effect that particle interactions have on wavefunction degeneracies.

Our treatment of the neutral donor involved thinking of it as a positively charged core plus *one* electron. The situation for the donor bound exciton is viewed in much the same way - a positively ionized core plus *two* electrons and *one* hole. Recall that the neutral donor described in Sec. 1.2 has a ground state with Γ_1 symmetry and two excited states with Γ_3 and Γ_5 symmetries (in the original shell model the splitting between Γ_3 and Γ_5 was considered negligible compared to the

splitting between Γ_1 and $\Gamma_{3,5}$).

Similarly, in the ground state, the two electrons in the donor bound exciton are in Γ_1 symmetric states and there are two empty excited states. The hole in the donor bound exciton has the symmetry of the valence band maximum, namely Γ_8. The donor bound exciton thus has a ground state configuration $\{2\Gamma_1;\Gamma_8\}$ (two Γ_1 electrons and one Γ_8 hole) and an excited state configuration $\{\Gamma_1,\Gamma_{3,5};\Gamma_8\}$ (one Γ_1 electron, one Γ_3 or Γ_5 electron and one Γ_8 hole). This model thus predicts the level scheme shown in Fig.1.3(a) for the donor bound exciton (the donor and acceptor bound excitons are labeled, respectively, as $D^\circ X$ and $A^\circ X$, while the neutral donors and acceptors are labelled D° and A°). The recombination of single electrons with single holes in the bound exciton leads to the transitions shown, i.e. a $\Gamma_{3,5}$ or a Γ_1 electron can recombine with the Γ_8 hole in the $\{\Gamma_1,\Gamma_{3,5};\Gamma_8\}$ state to give, respectively, a δ transition to the $\{\Gamma_1\}$ state or a γ transition to the $\{\Gamma_{3,5}\}$ state. One of the two Γ_1 electrons in the $\{2\Gamma_1;1\Gamma_8\}$ state can recombine with the Γ_8 hole to give a α transition to the $\{\Gamma_1\}$ state.

The bound exciton is labelled as an m=1 bound multiexciton complex. An m=2 donor bound multiexciton complex will be seen as a positively ionized core plus two holes and three electrons, an m=3 has three holes and four electrons, etc. The hole shell is four fold degenerate and will not be filled until m=4. The lowest electron shell is 2 fold degenerate and will be filled at m=1. For m=2 the third electron will go into a $\Gamma_{3,5}$ shell.

We have so far only considered structure due to electron states, i.e. valley-orbit splitting, and neglected possible structure due to the

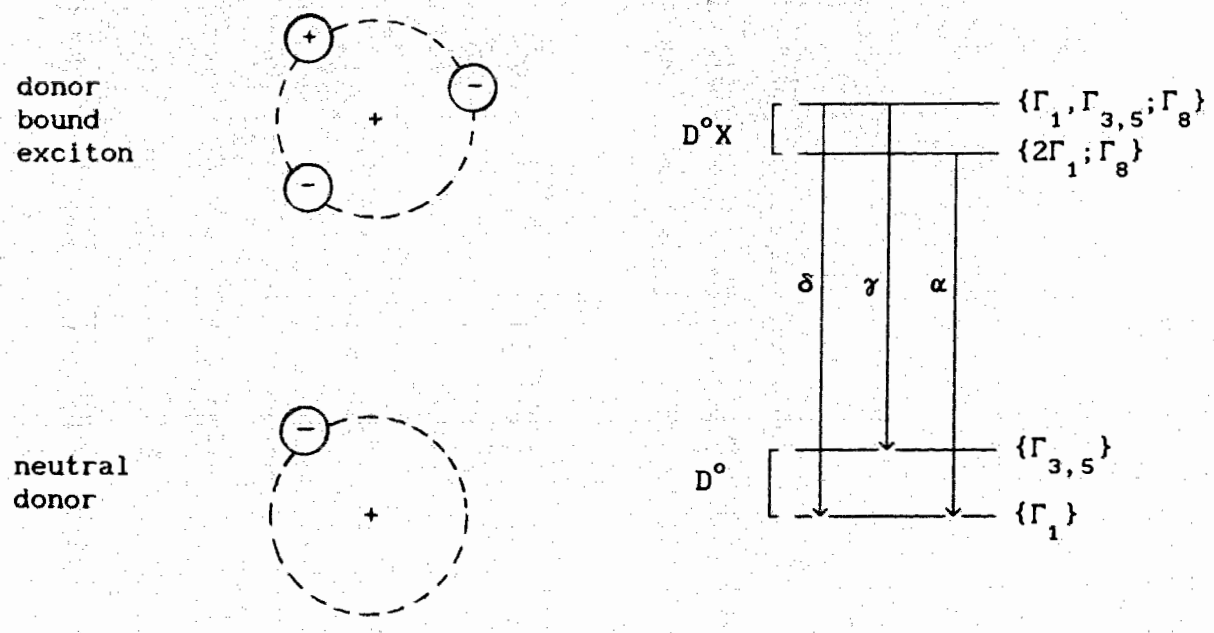

(a)

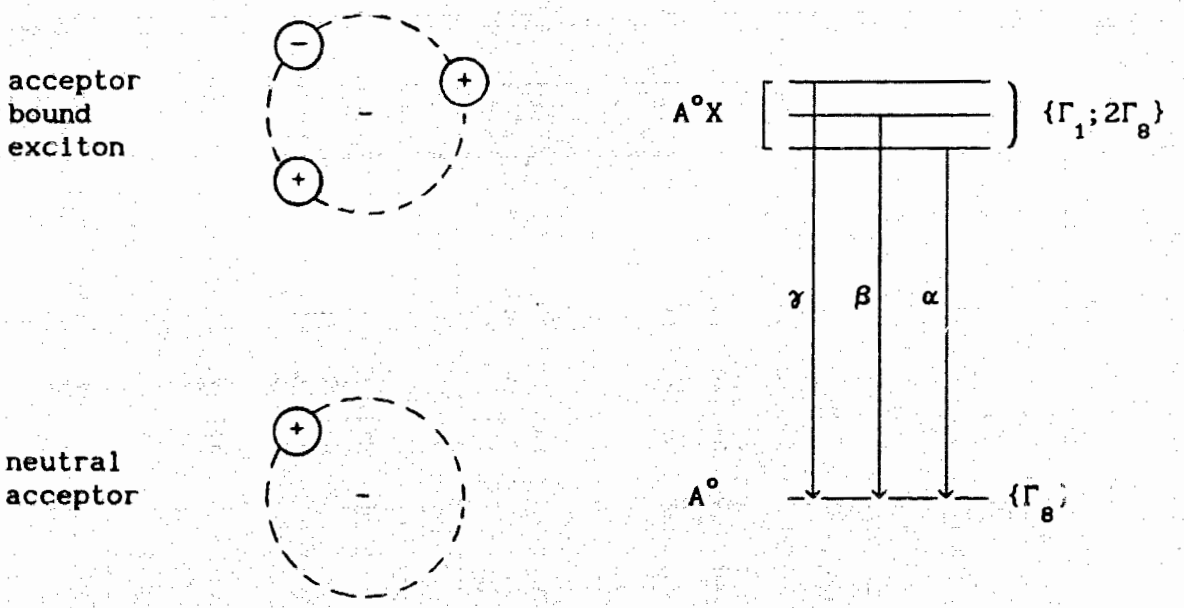

(b)

Fig. 1.3 Transition scheme for (a) the donor bound exciton and (b) the acceptor bound exciton

hole states. Since the hole in the donor bound exciton is repelled by the positive core, this is a fair consideration, given that the hole wavefunction will thus have a small amplitude near the core where the local strains, Stark fields and central cell potential due to the impurity will be largest. However, splitting of the hole states must be included in a description of acceptor bound excitons.

In contrast to the donor bound exciton, we visualize the acceptor bound exciton as a *negatively* ionized core plus *one* electron and *two* holes. In this case, the negative core *repels* the electron and *attracts* the holes. Thus for the acceptor bound exciton we expect a much reduced valley-orbit splitting of the electron states and we expect some structure due to splitting of hole states. As before, the holes start filling up a quartet of Γ_8 states. Valley-orbit splitting is considered negligible in the original shell model and thus the wavefunctions of electrons in acceptor complexes have the full symmetry of the conduction band. Experimental data at the time [77T1] [77T2] [77L] [76V] indicated a triplet structure of the acceptor bound exciton luminescence and an electron - hole *j-j* coupling scheme was originally adopted to describe this splitting [76V] [77L]. However, the observed intensities [77T2] [76V] [77L] of the bound exciton transitions did not agree with those predicted under such a scheme [73W] [77M]. In his presentation of the shell model, Kirczenow assumes that the splitting of the levels of the acceptor bound exciton is due to the interaction of two Γ_8 holes in the tetrahedral field of the impurity. $\{\Gamma_8 \times \Gamma_8\}$ contains three antisymmetric representations - Γ_1, Γ_3, and Γ_5 and thus the observed three fold splitting is explained without considering *e-e* and *e-h*

coupling. The scheme shown in Fig. 1.3(b) was proposed [77T2] to explain acceptor bound exciton luminescence.

In this model, we think of the bound exciton wavefunction as composed of individual non-interacting single particle states. Most splittings due to particle interactions and correlations are assumed to be smaller than the available resolution. To refine the shell model, it is necessary to consider all these possible couplings between the single particle states, and to take into account the small but perhaps not negligible splitting of the Γ_3 and Γ_5 electron states. Advancements in spectroscopic techniques render such refinement necessary if today's new higher resolution results are to be explained.

1.6 REVISIONS TO THE SHELL MODEL

The first approximation shell model discussed in in the previous section has recently been revised for the case of acceptor bound excitons [90K] [92K1] to include valley-orbit-splitting, and intra particle interactions more fully. This new model also includes terms to describe the effect of uniaxial stress on electron and hole wavefunctions. While the details are beyond the scope of this thesis, an attempt will be made here to present the essence of the theory. Its application to experimental results will be explored at the end of chapter four. A thorough discussion can be found in ref. [92K2].

A perturbation Hamiltonian describing the effects of stress, valley-orbit splitting, and particle interactions is constructed as a

function of several phenomenological parameters, using the symmetry of single particle states. The total Hamiltonian has the form

$$H = H_{vo} + H_{es} + H_{hs} + H_{hh} + H_{eh}. \qquad \text{eqn. (1.12)}$$

The first term, H_{vo} is expressed in terms of parameters Δ_1 and Δ_3 which characterize the difference in energy between the Γ_1 and Γ_5, and the Γ_3 and Γ_5 valley-orbit states, respectively. H_{es} describes the effect of uniaxial stress on electron states. H_{es} is diagonal for <111> stress, but for both <110> and <001> it is expressed in terms of the deformation potential constant of the conduction band. H_{hs} represents the effects of stress on hole states and involves the deformation potential parameters for the bound exciton. The last two terms H_{hh}, and H_{eh} describe intra-particle interactions.

The energy eigenvalues of the Hamiltonian yield the positions of the bound exciton energy levels. Constants Δ_1 and Δ_3 can be determined directly from experimental spectra, while values for the remaining parameters are obtained by best-fit comparison of the predicted energies to the observed energies.

CHAPTER TWO

EXPERIMENTAL TECHNIQUES

2.1 INTRODUCTION

The standard components in a system for studying photoluminescence are a dewar, an excitation source, a spectral analyzer, and a detector. In the case of stress studies, a mechanism of applying stress must also be included. Sample preparation varies depending on the specifics of the investigation - for studies which involve stress it can be a rather involved process.

Ultrahigh resolution spectra were collected from unstressed samples and from samples which were under uniaxial stress, at a resolution up to 2.5 μeV (0.02 cm^{-1}). This high resolution was possible primarily due to the use of a Michelson interferometer rather than a conventional dispersive instrument as the spectral analyzer. In the case of the stress study, full utilization of the high resolution afforded by the interferometer is possible only if the line broadening due to applied stress does not exceed the resolvable linewidth. Thus while the use of the interferometer was crucial to attaining high resolution spectra, a novel technique for sample fabrication and a specially built stress rig, which allowed us to make samples and stress them more uniformly than previous researchers, also contributed greatly.

2.2 FOURIER TRANSFORM SPECTROSCOPY

A conventional spectrometer collects a spectrum by scanning the wavelengths one after the other. In a Fourier transform spectrometer, however, spectra are collected by simultaneously sampling all wavelengths. For this purpose, a Michelson interferometer is utilized. Fig. 2.1 shows the basic Michelson set-up.

Light from a source S is divided by a beamsplitter into two beams, which are then reflected by the mirrors M_1 and M_2. The reflected beams interfere at the beamsplitter and are then incident on the detector D. Mirror M_1 is fixed and mirror M_2 is free to move, thus creating a difference x in the optical path length of the two split beams. The measured intensity I_{out} at the detector is then related to the incoming intensity I_{in} and the optical path length difference x by

$$I_{out} = \frac{I_{in}}{2} + \frac{1}{2}\int_{-\infty}^{+\infty} S(\lambda^{-1})\cos(2\pi\lambda^{-1}x)\,d(c\lambda^{-1}).$$

To obtain the spectrum $S(\lambda^{-1})$, we perform an inverse cosine Fourier transformation and get

$$S(\lambda^{-1}) = 2\int_{-\infty}^{+\infty} \left(I_{out} - \frac{I_{in}}{2}\right) \cos(2\pi\lambda^{-1}x)\,dx.$$

Due to practical limitations in the distance x that can be scanned, this

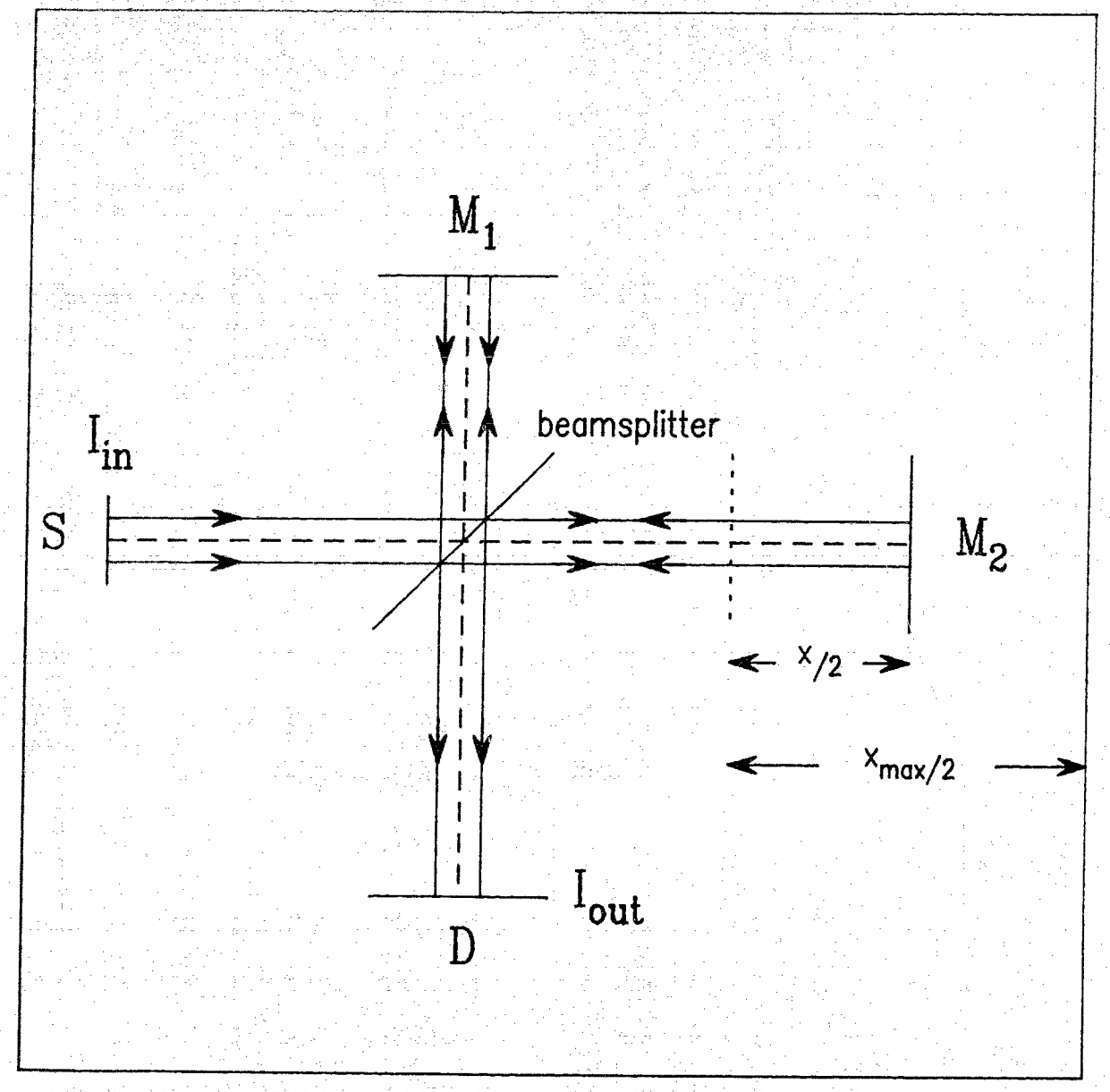

Fig. 2.1 A Michelson interferometer

integral must be restricted to a finite region, resulting in an observed linewidth that is broader than the actual width of a spectral component. This broadening is expressed in terms of the so-called "instrumental linewidth" and must be taken into account, if one attempts to determine the *actual* width of a measured feature.

The fact that we can sample all wavelengths simultaneously leads to the so-called multiplex or Fellgett advantage [86G]: N times as much time is spent at each wavenumber interval $[\lambda^{-1}, \lambda^{-1} + d\lambda^{-1}]$ as would be the case for the conventional dispersive spectrometer, when there are N such wavenumber intervals present. If the system noise is dominated by the noise of detector, i.e. the noise of the incoming intensity is negligible, this multiplex advantage enhances the signal-to-noise ratio by a factor of $\sqrt{N}$. How this advantage is maintained in our experiment will be described later.

Another benefit of interferometry is the so-called throughput or Jacquinot advantage [86G], which is due to the fact that the apertures used in an interferometer allow a much larger throughput of radiation than those of a dispersive instrument, i.e. the long narrow entrance slit of a conventional dispersive instrument has a smaller area than an interferometer's circular apertures. This benefit is especially valuable in experiments such as ours which require high resolution.

The interferometer used in these studies was a Bomem DA3.01 model. This model has intrinsic characteristics of its own that set it apart from some other commercially available interferometers. The most important one for our purpose is its dynamic alignment system, which maintains mirror alignment ($M_1 \| M_2$) over a large scanning range and

facilitates the collection of ultrahigh resolution spectra. A more thorough discussion of the Bomem interferometer and its use in this lab has been presented elsewhere [90T].

2.3 SAMPLE PREPARATION AND MOUNTING

2.3.1 Zero-stress Samples

Preparing and mounting the samples used in the zero stress studies was relatively straightforward. The samples were pieces of wafers previously cut from single crystals of float-zone silicon with different impurity concentrations. The sample shape and size varied, but had a typical dimension of 20 x 20 x 5 mm^3. Before being mounted the samples were cleaned with acetone, then ethanol, and etched in a 5:1 mixture of concentrated HNO_3 and HF to remove any surface damage or oxide layers. Samples were mounted in a stress-free manner by using teflon tape to attach them flat to a piece of aluminum that was suspended in the dewar by a rigid rod.

2.3.2 Stress Samples

Samples were prepared from single crystals of high purity silicon having a boron concentration of $3x10^{15}cm^{-1}$ and some low phosphorous concentration. The silicon was first cut in the shape of a roughly rectangular parallelepiped with one side along a known (from x-ray

diffraction) crystallographic direction. To bring the sample to the finished form shown in Fig.2.2, the other three sides had to be adjusted, so that all sides had equal widths and met at right angles. The ends were pyramids with points axial to the body of the sample, requiring the use of a special polishing jig which is shown in Fig.2.3. The samples were attached to the rig using a wax-like substance. Mounting the sample involved heating the jig, melting the adhesive, positioning the sample, then cooling the apparatus. To remove the sample, the jig was heated, the samples was removed and both the jig and the sample were thoroughly cleaned with acetone.

Once mounted, polishing the sample involved manually moving the polishing face of the jig (labelled in Fig.2.3) over a polishing surface, e.g. "sand" paper or a diamond paste. The sides were finished first. The stage was adjusted so that when the oriented side of the sample was pressed against it, the opposite side extended just past the polishing face of the jig, as shown in Fig.2.3(a). A 400 grit sandpaper was used to bring the sample edge almost flush with the polishing face, then the sample was turned 90^{0} and the procedure was repeated, then turned 180^{0} and the last face polished. At this point the body was close to having the desired shape. A 1μm diamond paste was employed to bring the sides flush with the polishing face and remove the surface damage caused by the sandpaper. The final dimensions were approximately $2 \times 2 \times 20$ mm^{3}.

The opposite end of the polishing jig was used to put the pyramids on the sample. One end of the sample was pressed against the stage and the other overhung the angled polishing face, as shown in Fig.2.3(b).

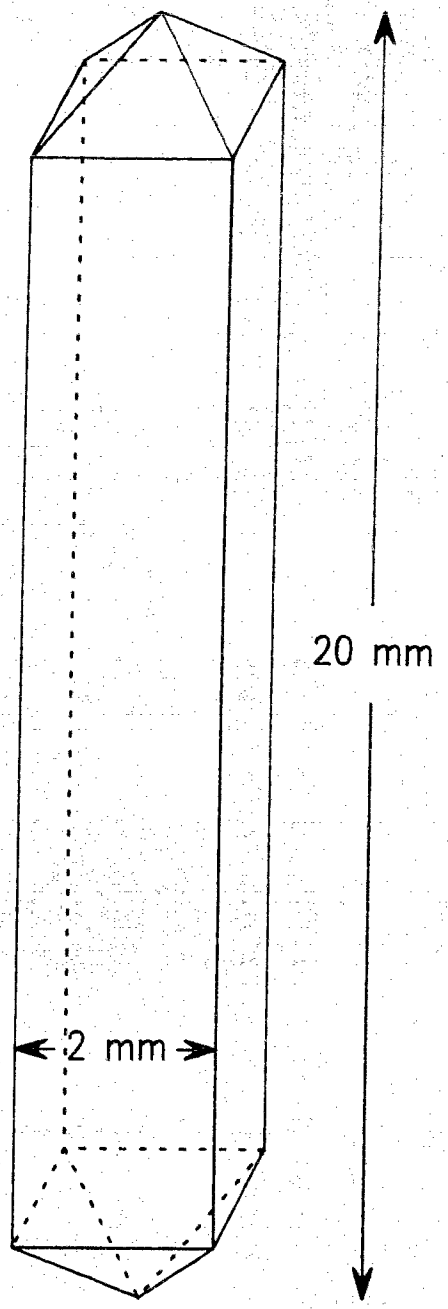

Fig.2.2 Stress sample geometry

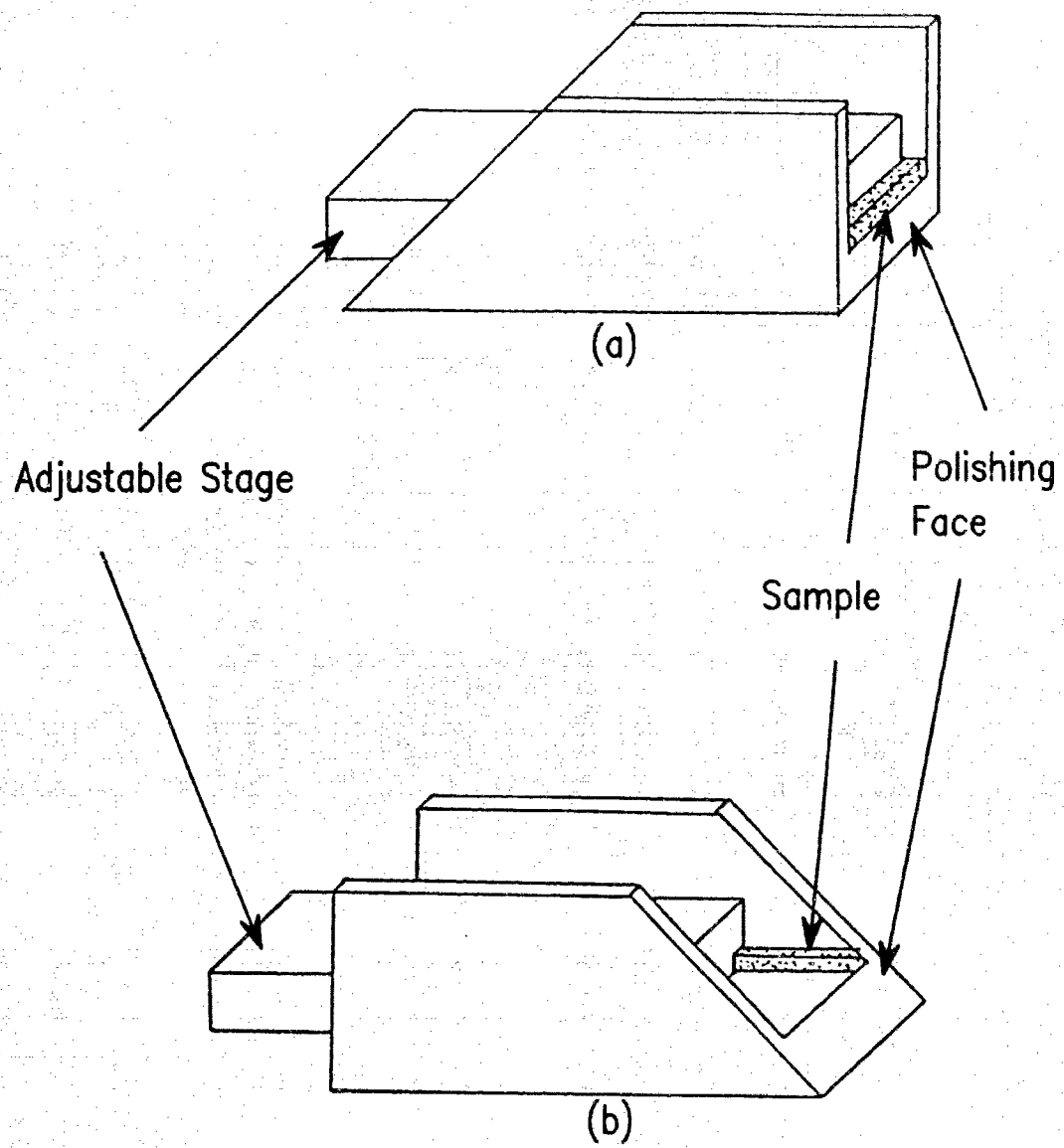

Fig.2.3 Polishing jig

As illustrated in Fig.2.4, this geometry put four faces on each end. Each face was polished with 600 grit sandpaper to bring it into shape, then 1μm diamond paste was again used to finish the surfaces. The stage was fixed throughout this process and the polishing angle remained constant, thus ensuring that the four faces met at a single point.

While this method was fairly straightforward, a number of factors slowed down the process and often led to less than ideal samples. The main setback laid in the difficulty in ensuring that the sample rested flat against the jig each time it was mounted, and that each side was polished flush (or at least flush to the same extent) with the polishing face. In addition, the sample was easily chipped when handled which increased the amount of time needed to produce a "good" sample; good samples were those that could be uniformly stressed, and the better the surface finish the more uniform the stress. On average, a couple of days were required to prepare a sample having the desired symmetry and surface quality. The samples were etched in a 5:1 HNO_3:HF solution to remove surface damage before being mounted in the stress rig.

2.3.3 Stress Rig

The stress rig consists of two parts, as shown in Fig.2.5. The top part is about 100 cm long and is basically a cylindrical shell with an inner centered "stress rod" which can be pushed on from above by placing weight on a platform in contact with it. This top portion is rather unremarkable - it is the bottom that is essential to obtaining good stress.

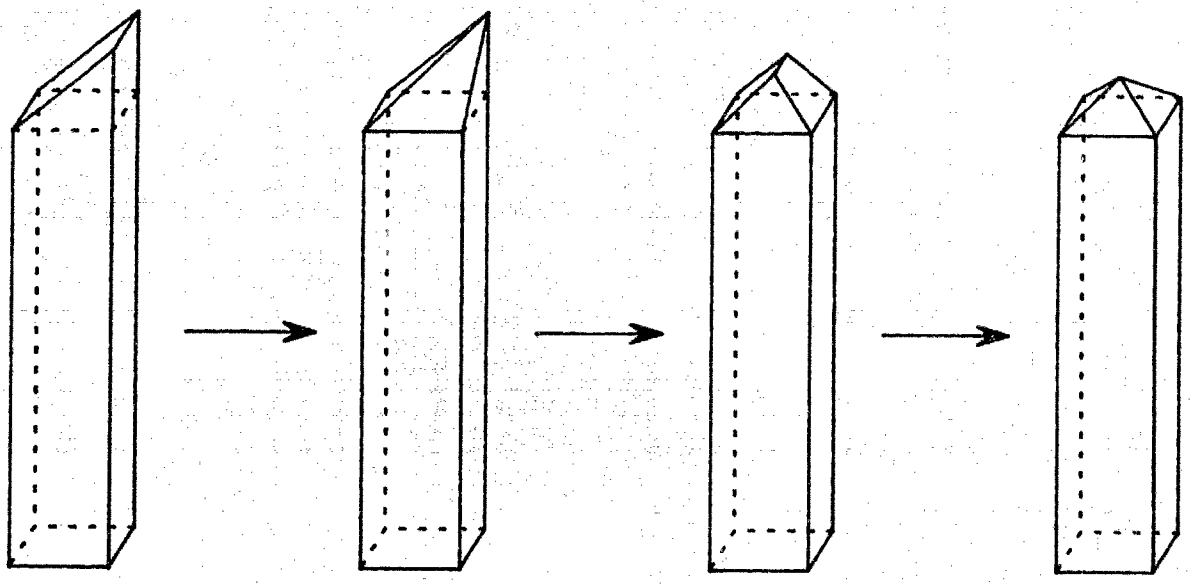

Fig.2.4 Steps in bringing the sample to the finished form

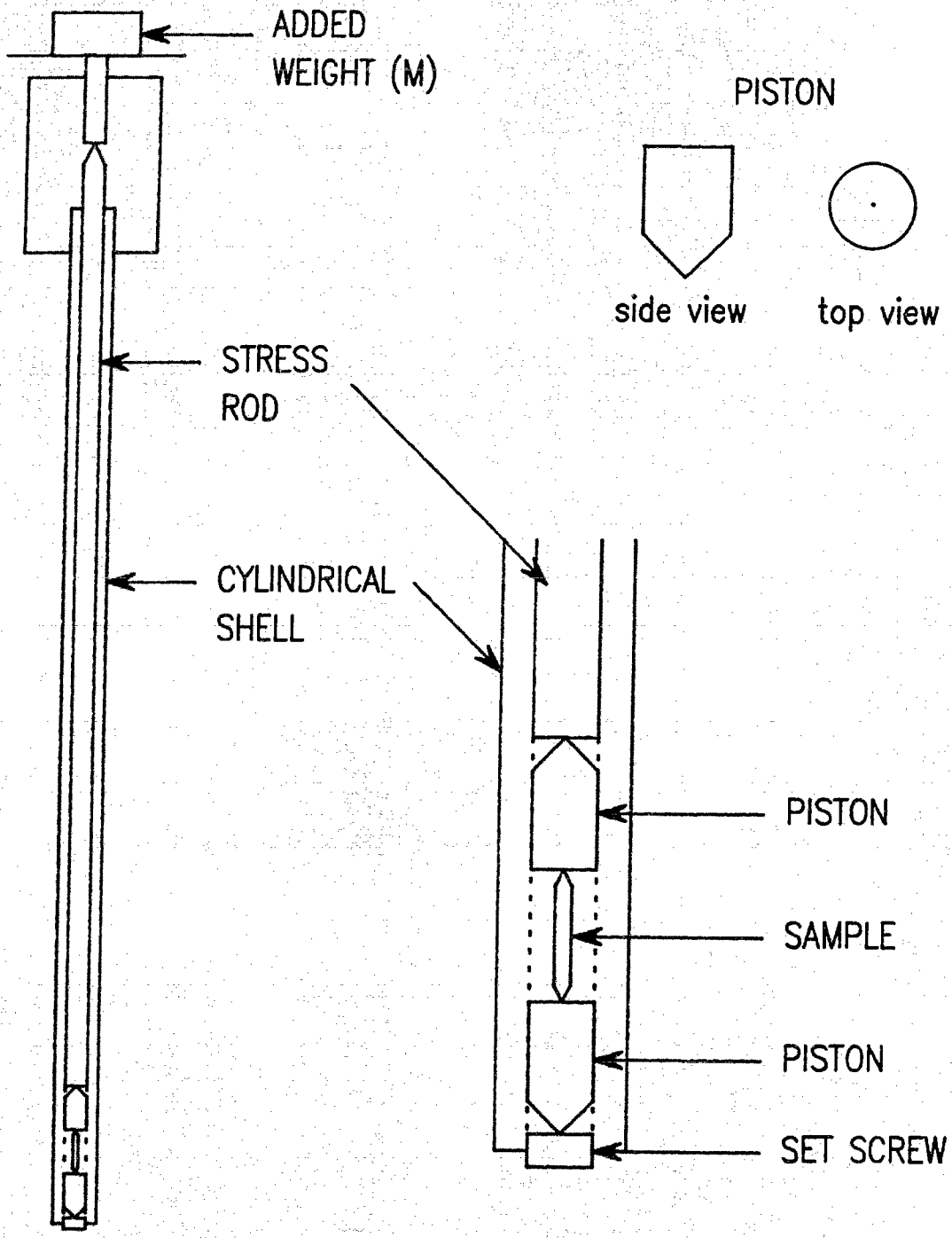

Fig.2.5 Stress rig

Two cylindrical pistons, an adjustable set screw, and a cylindrical shell make up the bottom piece, as shown in Fig.2.5. The sample is mounted between the two pistons and stress is applied to it by pressing the stress rod against the top piston. Fig.2.5 also shows the design of a piston. One end is flat with a dimple stamped in the center and the other end is conical. The points of the sample fit into the dimples such that the sample is held vertically in the center of the rig. Easy mounting of the sample is facilitated by the set screw which can be used to raise or lower the bottom piston and thus vary the space available for the sample. The point of the top piston is in contact with the stress rod and the point of the lower piston rests against the set screw. Provided that the point of each cone is axial with the body of each piston, and the pistons are snugly centered inside the shell, the cone-head design should ensure that the stress is applied uniformly. Since both the dimples in the pistons and the points of the sample are axially aligned, this mounting geometry should permit uniform uniaxial stress to be applied, especially in the center of the sample.

The main difficulty in using this stress rig lies in its tendency to "seize up". Gas trapped in the movable parts can freeze and often make the rig unusable until it can be warmed up - a tedious task when working in liquid helium. As well, the rig can freeze but go unnoticed as additional weight is added to the stress rod. The extra weight can often loosen the "ice" with the consequence of the entire mass crashing onto the sample. Obviously this is not a desirable scenario as this can chip the sample or shatter it entirely.

2.4 PROCEDURE

Fig. 2.6 shows the experimental setup. The mounted samples were placed in a standard immersion dewar. The sample chamber was filled with liquid helium and pumped to below the lambda point (2.18 K). The pumping was done primarily to reduce the noise caused by light scattering off bubbling helium, thus maintaining our multiplex advantage. Excitation was provided by a stabilized 500 mW argon ion laser or by a 500 mW titanium sapphire laser tuned to ~900 nm (1.4 eV).

In most cases the light was focused onto the crystal face and the signal was collected off the edge. An off-axis parabolic mirror, M, collimated the signal and directed it into the interferometer through a 12 cm quartz window, W. An internal white light source could be directed back through the interferometer and onto the sample to enable alignment of the sample with the optics. The white light reference beam, and stray excitation laser light were removed after leaving the interferometer by a combination of optical filters. A 1 mm diameter InGaAs photodiode cooled to 77 K and sensitive in the range 800 - 1500 nm (1.5 - 0.8 eV) detected the interference signal. From the detector, the signal was amplified and converted to a digital one, which was subsequently sent to the computer for Fourier transformation.

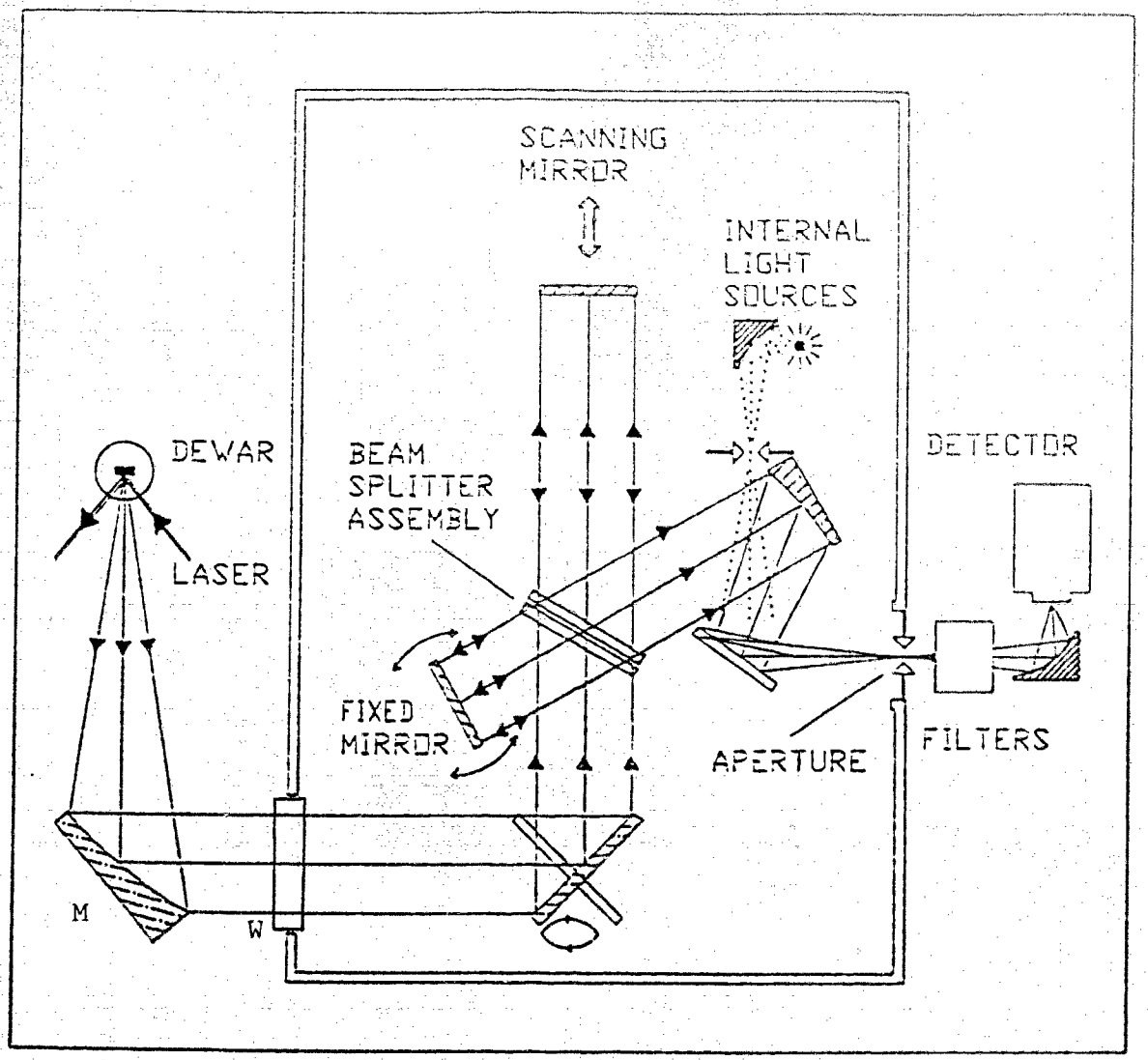

Fig. 2.6 Experimental setup

CHAPTER THREE

BOUND EXCITON FINE STRUCTURE AT ZERO STRESS

3.1 INTRODUCTION

This project began with an ultra-high resolution study of the zero stress bound exciton spectra of the donors phosphorous and arsenic and the acceptors boron, aluminum, gallium, and indium, in silicon. Photoluminescence spectra were collected in the no-phonon region with unparalleled resolution (up to 2.5 μeV) and single-to-noise ratio.

The donor bound exciton spectra, presented in Sec. 3.2, consist of a single feature whereas the acceptor bound exciton spectra, presented in Sec. 3.3, all have extensive fine structure. In both these sections, the spectra are discussed in terms of the conventional shell model.

3.2 DONOR BOUND EXCITONS

The bound exciton spectra of the two donors studied, phosphorous and arsenic, have no fine structure and can be completely explained within the Shell Model. Fig. 3.1 shows the phosphorous and arsenic bound exciton spectra along with the proposed energy level diagram and transition scheme. As discussed earlier, the electrons in the neutral donor and donor bound exciton can be found in either a two-fold

degenerate Γ_1 level, a four-fold degenerate Γ_3 level or a six fold degenerate Γ_5 level, where Γ_1 is the ground state and Γ_3 and Γ_5 are excited levels. The Γ_3 and Γ_5 levels are separated from the ground state by a few meV and thus are unpopulated at liquid helium temperatures. Since the hole in the bound exciton is in a Γ_8 state, the bound exciton will have a configuration $\{2\Gamma_1;\Gamma_8\}$, while the neutral donor which has no hole will have configuration $\{\Gamma_1\}$.

No extra splittings due to interparticle interactions are anticipated in this case. In the initial state, the two Γ_1 electrons form a spin singlet which does not cause any splitting when it interacts with the Γ_8 hole, while in the final state the electron is in a Γ_1 level whose only degeneracy is due to spin. The unpopulated $\Gamma_{3,5}$ states are ignored as possible initial states of a transition, although the excited levels can act as final states of transitions from higher order BMECs.

This model thus predicts a single transition, α, from the initial $\{2\Gamma_1;\Gamma_8\}$ state (the bound exciton) to the $\{\Gamma_1\}$ final state (the neutral acceptor), as indicated in Fig. 3.1.

The observed full-width-at-half-maximum (FWHM) for the phosphorous bound exciton, taken at an instrumental linewidth of 2.5 μeV, was 5.7 μeV which corresponds to a actual FWHM of 5.1 μeV. This compares well with the previous estimate of 5 μeV [81K2]. The observed FWHM for the arsenic bound exciton line, taken at an instrumental linewidth of 6.2 μeV, was 11.4 μeV which corresponds to an actual FWHM of 9.9 μeV.

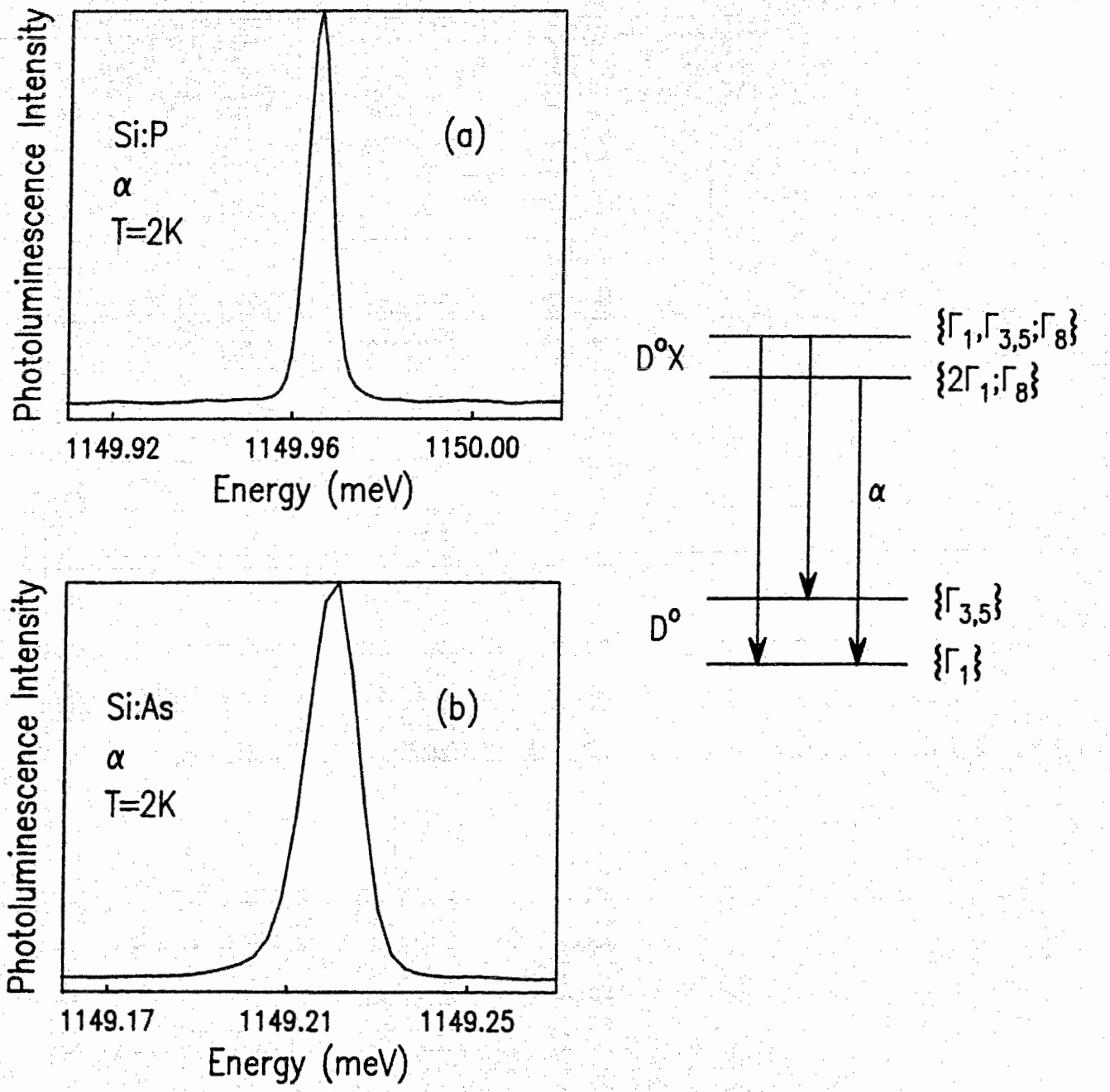

Fig. 3.1 (a) Phosphorous and (b) arsenic bound exciton luminescence at zero stress. The diagram on the right shows the predicted energy levels and the possible transitions.

3.3 ACCEPTOR BOUND EXCITONS

The acceptors boron, aluminum, gallium, and indium all have extensive bound exciton fine structure, most of which can not be explained by the conventional shell model. As discussed earlier, the neutral acceptor has one hole in a Γ_8 shell. The electron in the BE is in a six-fold degenerate (twelve-fold counting spin) shell and the two holes occupy a Γ_8 shell. The two Γ_8 holes couple and the level splits into Γ_1, Γ_3, and Γ_5 states ($\{\Gamma_8 \times \Gamma_8\} = \Gamma_1 + \Gamma_3 + \Gamma_5$). Γ_1 is lowest in energy and forms a two hole-state ground state which does not produce any additional fine structure when it interacts with the electron. This scheme allows three transitions, α, β, and γ, one from each of the three states in the bound exciton to the single neutral acceptor state (at liquid helium temperatures, only the ground state transition, α, is observed for acceptors gallium, aluminum, and indium, since the splitting between levels is large compared to kT). This was the proposal of the original shell model and it was sufficient to explain the experimental results of the time. Since then, however, additional fine structure on the α line has been reported [78E3], [83K], [88G].

The most recent studies prior to ours had revealed three fine structure components for Al, two for Ga, and two for In [88G]. This structure was explained in terms of valley orbit splitting of electron states together with the Γ_1 two-hole state [88G]. Our spectra of the aluminum, gallium, indium and boron bound excitons, are shown in Figs. 3.2 and 3.3. The alphabetical labels are arbitrary and refer to the energies quoted in Table 2 for the positions of the fine structure

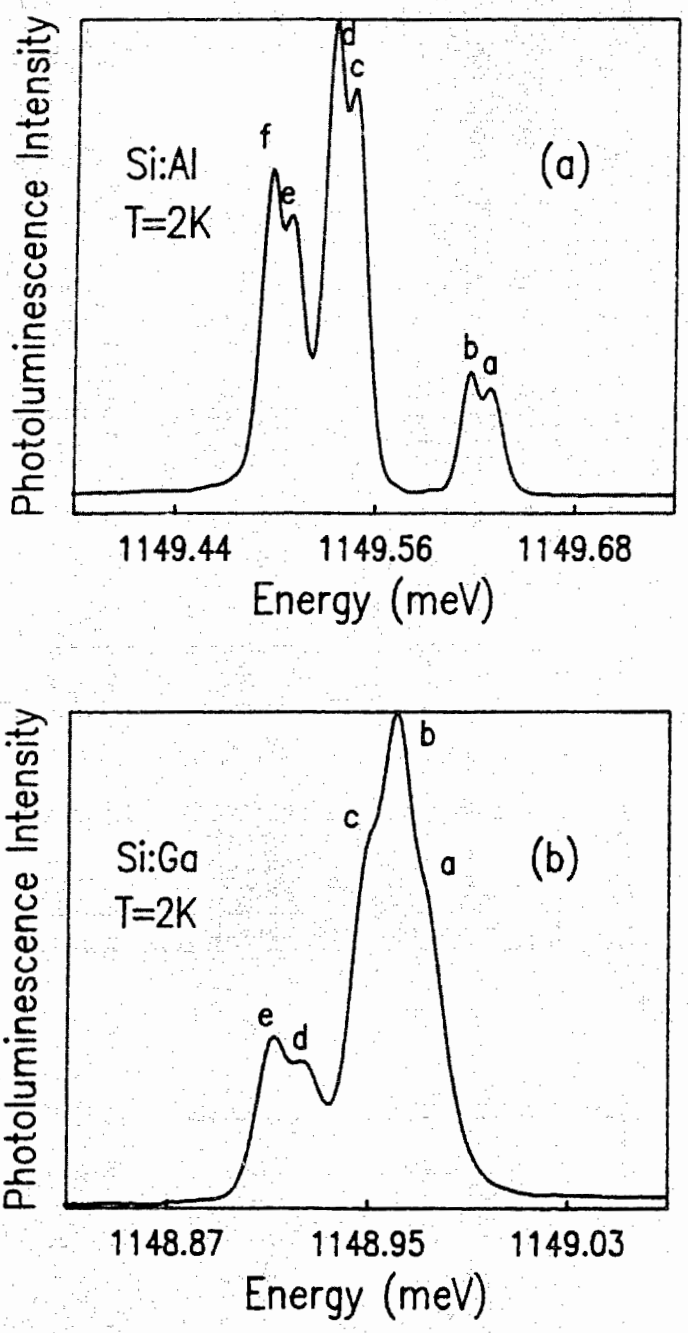

Fig. 3.2 (a) Aluminum and (b) Gallium bound exciton luminescence at zero stress.

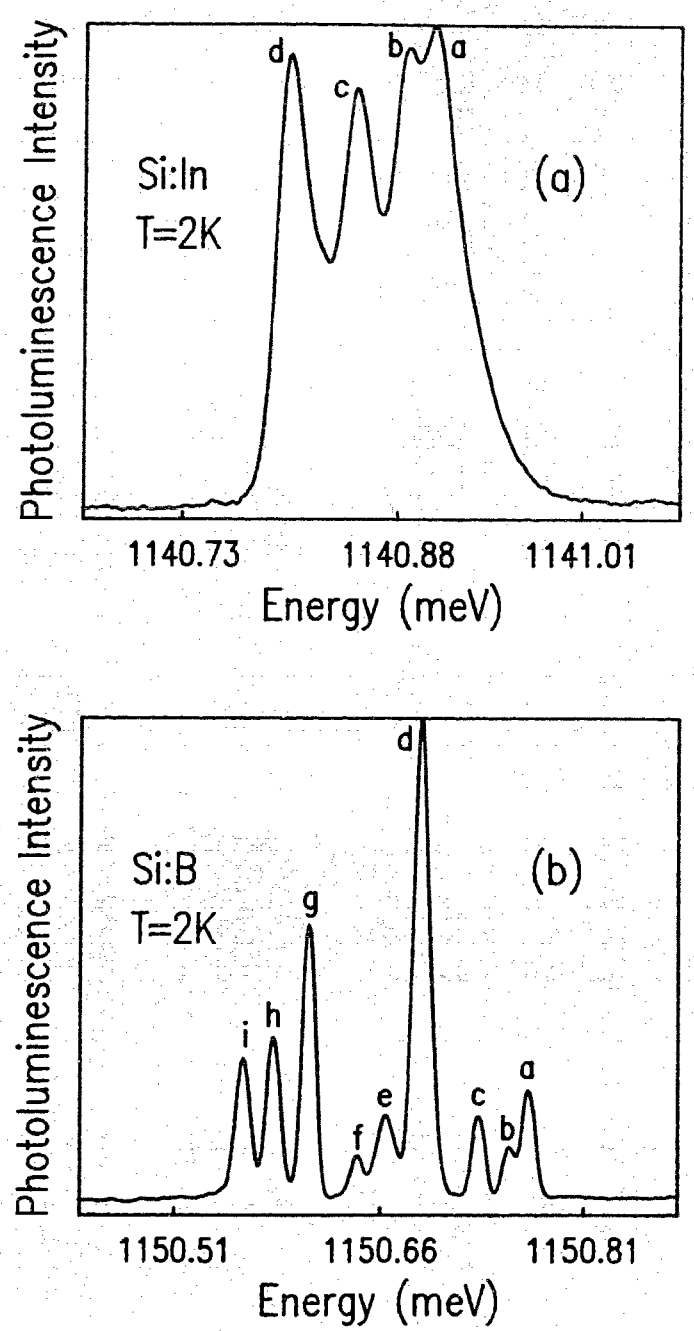

Fig. 3.3 (a) Indium and (b) boron bound exciton luminescence at zero stress.

TABLE 2

Impurity	Label	Energy (cm^{-1})	Energy (meV)†
Boron	a	9281.59 ± 0.03	1150.771 ± 0.004
	b	9281.47	1150.756
	c	9281.28	1150.732
	d	9280.94	1150.690
	e	9280.73	1150.664
	f	9280.56	1150.643
	g	9280.27	1150.607
	h	9280.07	1150.582
	i	9279.89	1150.560
Aluminum	a	9272.28 ± 0.03	1149.616 ± 0.004
	b	9272.40	1149.631
	c	9271.73	1149.548
	d	9271.62	1149.534
	e	9271.43	1149.511
	f	9271.32	1149.497
Gallium	a	9267.10 ± 0.03	1148.974 ± 0.004
	b	9267.00	1148.962
	c	9266.90	1148.949
	d	9266.71	1148.926
	e	9266.60	1148.912
Indium	a	9202.03 ± 0.03	1140.906 ± 0.004
	b	9201.84	1140.883
	c	9201.58	1140.851
	d	9201.20	1140.803
Phosphorus		9275.10 ± 0.03	1149.966 ± 0.004
Arsenic		9269.08 ± 0.05	1149.219 ± 0.006

† $1\ cm^{-1} = \left(\frac{h\ c}{e} \times 10^{5} \right)$ meV = 0.1239842 meV
(using the most recently determined values of h, c, and e [ref. 91C])

lines.

The aluminum bound exciton displays the coarse triplet structure ofthe previous study [88G], but in addition each triplet component is split into an identical doublet. The structure of the gallium bound exciton displays a coarse doublet splitting, but there is at least a two-fold splitting associated with one of the lines and possibly a three fold splitting with the other. Our spectrum for indium displays five components which is irreconcilable with the previous study [88G]. No explanation of this fine structure can be reasonably attempted until further studies are undertaken.

Boron has been the least studied of these acceptors, due most likely to the low intensity of boron related photoluminescence in the no-phonon region which makes conventional spectroscopy very difficult. One of the few boron bound exciton studies using conventional spectroscopy revealed three barely resolvable fine structure components [78E3], while a more recent study in which a dispersive instrument was coupled to a Fabry-Perot interferometer [83K] has revealed a more complicated structure. Our study reveals at least nine well resolved components. An interpretation of this structure in light of our stress study is presented in the following chapter. Our zero-stress spectrum of the boron bound exciton is shown in Fig.3.3(b). Again, the labels are for reference with Table 2.

3.4 CONCLUSION

Ultrahigh resolution spectra of donor and acceptor bound excitons in silicon have been collected for the first time. The linewidth and position of both the phosphorous and arsenic bound exciton line have been determined. Positions of the fine structure components of the bound exciton lines of the acceptors boron, aluminum, gallium, and indium have been tabulated.

The donor spectra can be explained by the existing shell model while the acceptors all show structure which currently can not be understood in that context. Further discussion of the boron bound exciton spectrum is the subject of the following chapter.

CHAPTER FOUR

BORON BOUND EXCITON FINE STRUCTURE UNDER UNIAXIAL STRESS

4.1 INTRODUCTION

As discussed in Sec. 1.2, applying stress along the crystallographic axes <111>, <110>, and <001> will remove degeneracies from the conduction and valence bands in a predictable way. Since the collective electron and hole wavefunctions which describe the bound exciton are chosen from near the band edges, the removal of conduction and valence band degeneracies will in turn split the bound exciton energy levels.

The next section will describe the method for calibrating the applied stress. The results of the stress experiments along with some interpretation will be presented in Sec. 4.3. In the last section, a comparison of these results with those predicted by the new model of the acceptor bound exciton will be made and some conclusions will be drawn.

4.2 CALIBRATION OF STRESS

The stress, S, on the sample is given as

$$S = \frac{F}{A} \qquad \text{eqn. (4.1)}$$

where F is the effective force applied to the sample and A is the cross sectional area of the sample. However, referring back to Fig.2.5, it is clear that the weight, Mg, applied to the top of the stress rig is not equal to F. Rather, the mass of the rod, the mass of the upper piston, friction between the different components, etc., will contribute to a force f which must be added to the weight Mg to give the total force

$$F = Mg + f \qquad \text{eqn. (4.2)}$$

An estimate of the stress can be made by approximating the size of f in eqn. (4.2). However this is not always convenient, since f can vary from spectrum to spectrum. Instead, in these experiments S was determined by measuring the splitting, ΔP, of the phosphorous bound exciton line in the spectrum (recall that there is a low concentration of phosphorous in the samples). Since we know from the literature [78K] that the phosphorous bound exciton line splits linearly with stress ($S = K\Delta P$), we can calibrate the stress by measuring the splitting as a function of applied mass, M, as shown in Fig.4.1. Assuming that f does not depend on M, we can determine the constant of proportionality as

$$K = \frac{g}{m\,A} \qquad \text{eqn. (4.3)}$$

where g and A are defined above and m is the slope of the line in Fig.4.1, obtained by a linear regression. For stress along the <111> direction m = 0.085 meV·kg^{-1}, and so if the cross sectional area of the

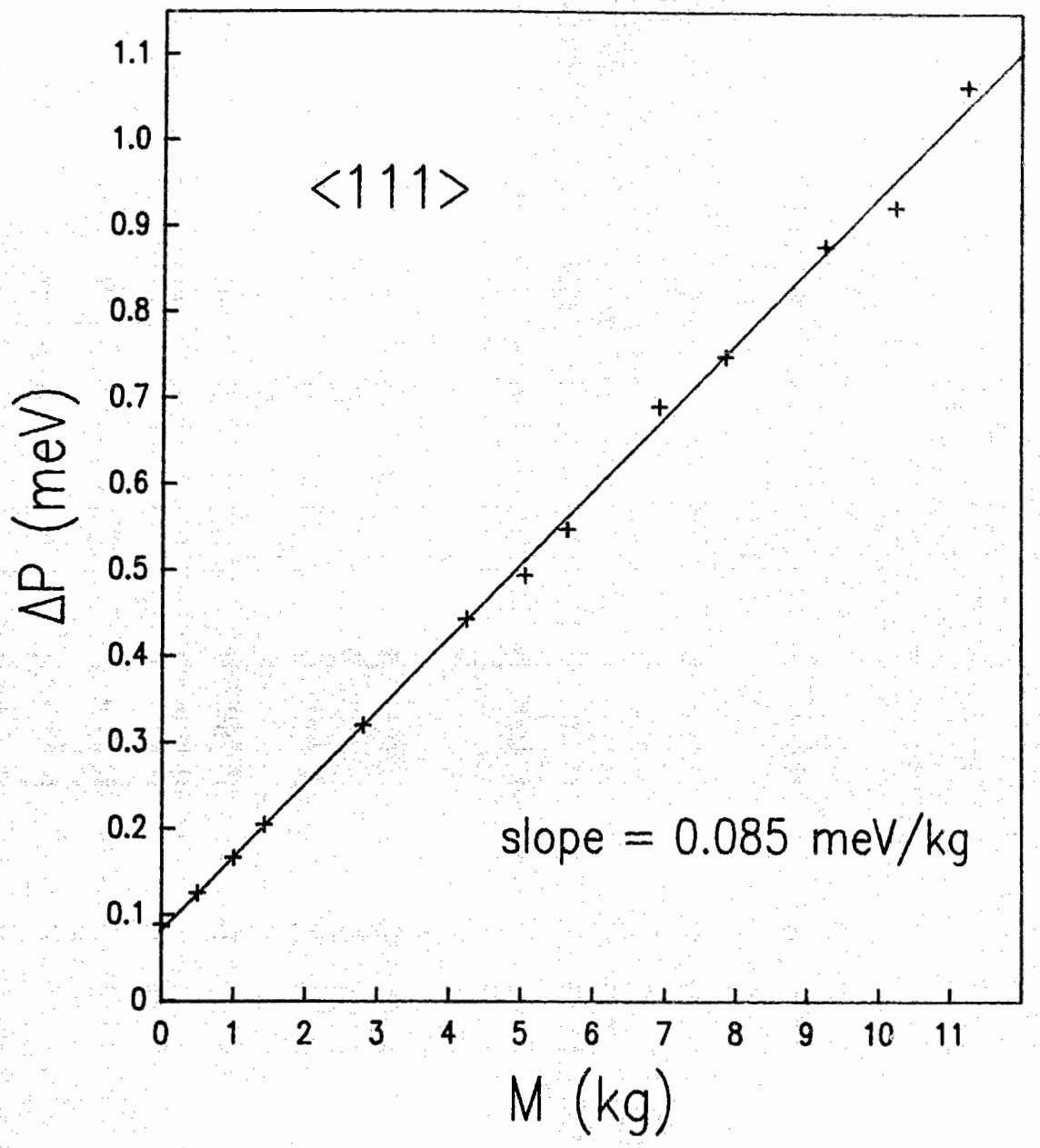

Fig. 4.1 Splitting, ΔP, of the phosphorous bound exciton line as a function of added mass M.

sample is $4mm^2$, $K = 2.9 \times 10^7$ Pa·meV^{-1}. This value is in agreement with a previously quoted value [78K] of $K \sim 3 \times 10^7$ Pa·meV^{-1}.

We now can measure the magnitude of the stress on the sample by looking at the spectrum and measuring ΔP (in meV), i.e.

$$S = 29\Delta P, \qquad \text{eqn. (4.4)}$$

where S is measured in MPa. The magnitude of K for stress along the <110> and <001> directions was determined in the same way and found to be $K = 2.9 \times 10^7$ Pa·meV^{-1}, and $K = 2.7 \times 10^7$ Pa·meV^{-1} respectively.

4.3 RESULTS AND DISCUSSION

4.3.1 Making an energy level diagram

The neutral acceptor level is split into two levels under uniaxial stress; hence to create an energy level diagram of the bound exciton, it is necessary to distinguish between transitions which terminate at the upper level of the neutral acceptor and those which terminate at the lower level. As seen in Fig. 4.2, for each bound exciton energy level, we can possibly see two spectral lines. The splitting of the neutral acceptor level is labelled Δd, and is linear with applied stress. Transitions to the upper, $m_j = \pm 3/2$, neutral acceptor level (labelled u) are denoted $X_{\#}^{u}$ while those to the lower, $m_j = \pm 1/2$, level (labelled ℓ) are denoted $X_{\#}^{\ell}$, where # indicates the (arbitrarily labelled) bound exciton

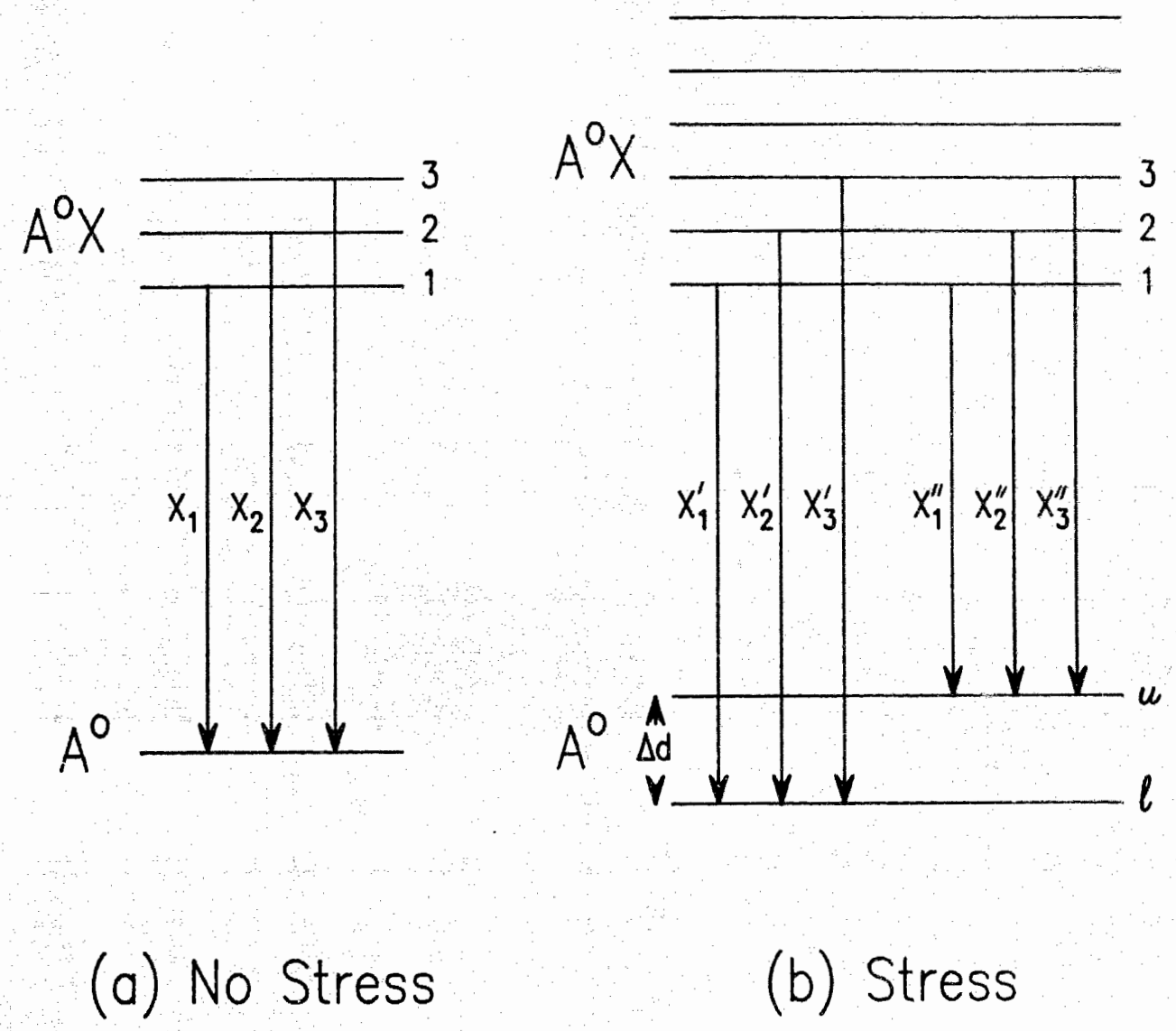

Fig. 4.2 Possible transitions from the boron bound exciton energy levels to the neutral acceptor levels when (a) no stress is applied and (b) stress is applied. Δd is the splitting of the neutral acceptor level.

energy level.

Fig. 4.3 shows the bound exciton photoluminescence when a stress of 10.6 MPa is applied along the <111> direction. Transitions which originate from the same energy level are identified by determining which components are separated by the same energy (a trial and error process). For example, in Fig. 4.3, components X_1'' and X_1', X_2'' and X_2', X_3'' and X_3', etc. are all separated by the same amount, Δd, and represent transitions from energy levels 1, 2, 3, etc.

Unfortunately, which components can be paired is not always obvious. At low stress, both the bound exciton energy levels and the neutral acceptor energy levels are closely spaced and so transitions between these levels will have very similar energies. In the photoluminescence spectrum, this will manifest itself as many closely spaced components, many of which will overlap each other. In addition, it is possible that either the transition to the upper or the lower neutral acceptor level will be missing from a spectrum and so from a single spectrum alone it is impossible to ascertain if the transition is X'' or X'.

So-called "fan diagrams" are created to aid in the pairing of components. These diagrams are created by compiling the spectra at different stresses to give a plot of spectral line position as a function of stress. Fig. 4.4 shows the bound exciton photoluminescence spectrum at three different stresses along the <111> direction, plus the associated <111> fan diagram. The points on the fan diagram at 10.6 MPa (marked with the "*") indicate the positions of transitions in the photoluminescence spectrum shown previously in Fig. 4.3. Transitions X_1''

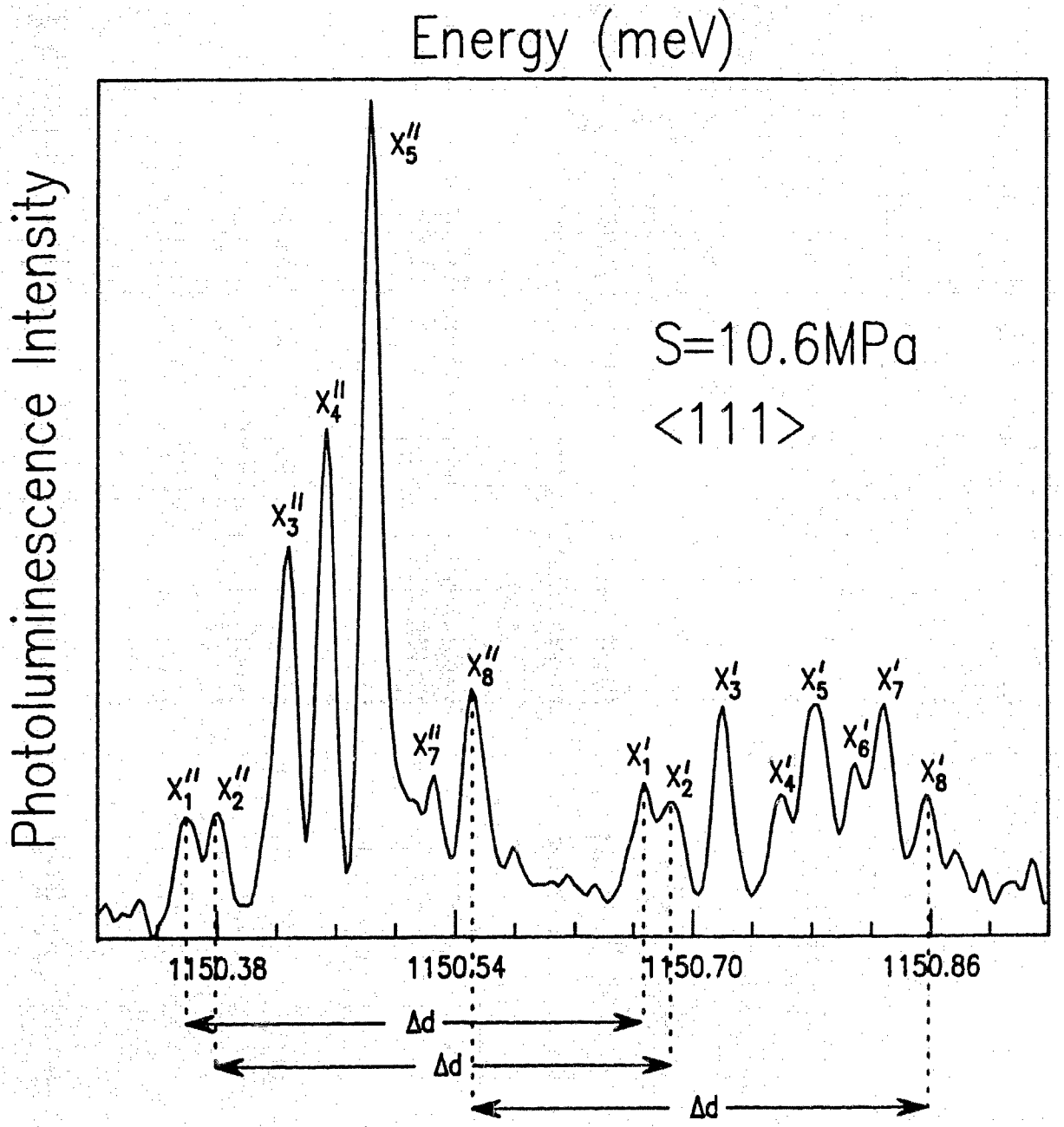

Fig. 4.3 Boron bound exciton luminescence when a stress of 10.6 MPa is applied along the <111> direction.

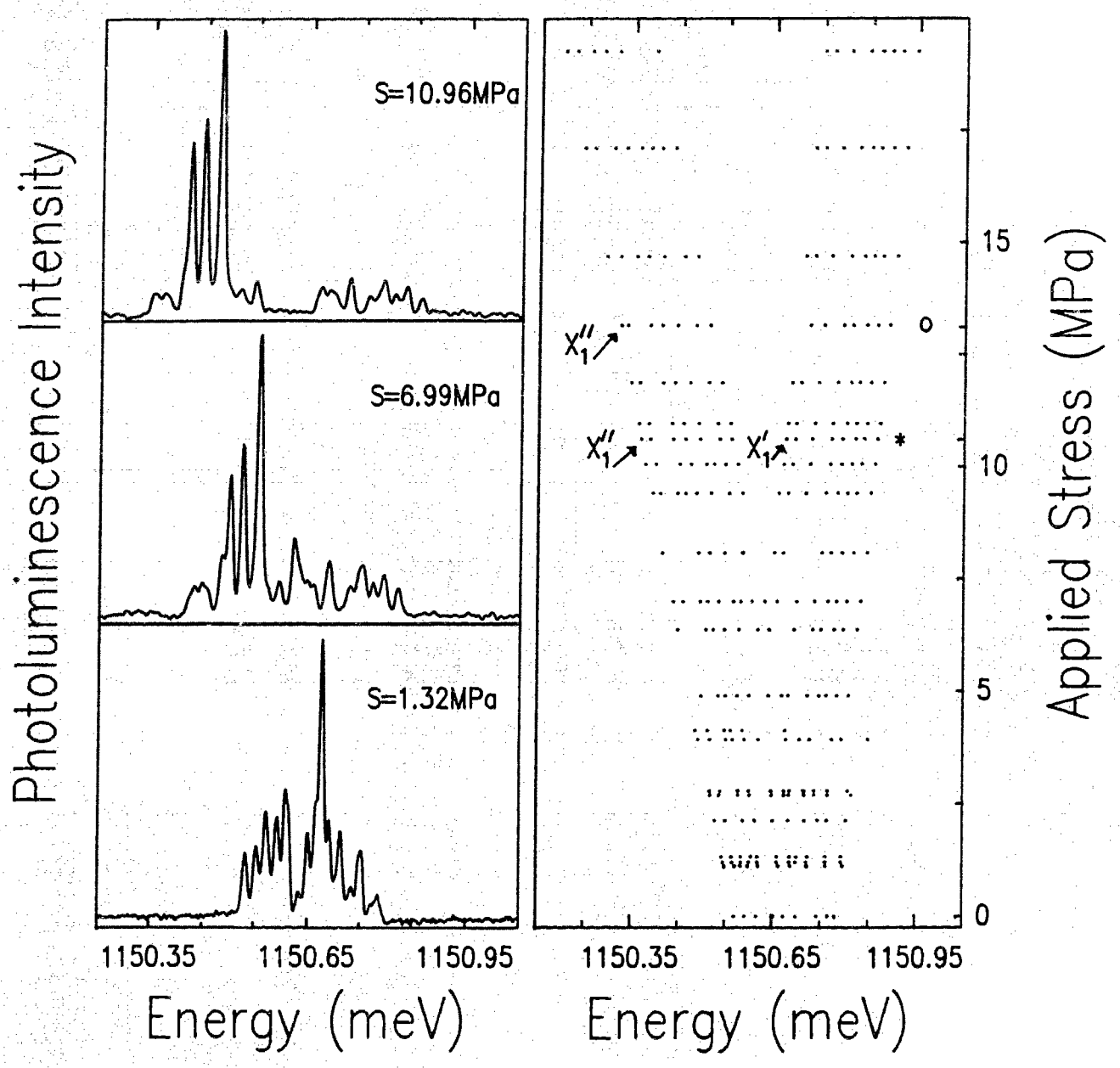

Fig. 4.4 (a) Boron bound exciton luminescence when three different stresses are applied along the <111> direction. (b) <111> fan diagram.

and X_1' from Fig.4.3 are labelled on the fan diagram as well. Put in the context of a fan diagram, each spectrum can be interpreted more generally. For example, even if in the 13.1 MPa spectrum (marked with the "o") the transition from energy level "1" to the lower neutral acceptor level did not appear, the transition to the upper energy level could still be identified by tracing the evolution of transition X_1'' in the fan diagram. In conjunction with analyzing the fan diagram, at low stress it is also necessary to look closely at the spectra and note changes in both line position and intensity with very small increments of stress in order to trace each spectral line and thus identify it as originating from either a X'' or a X' transition..

The energy of the bound exciton levels can be obtained by adding $\Delta d/2$ to the X'' transitions or subtracting $\Delta d/2$ from the X' transitions (if the transitions have been labelled correctly, $(X'' + \Delta d/2)$ will be equal to $(X' - \Delta d/2)$). Fig.4.5 is the bound exciton energy level diagram as a function of stress along the <111> direction (the lines represent the predicted energy levels and they will be discussed in Sec.4.4). Similar results were obtained for stress applied along the <110> and the <001> directions.

4.3.2 Determining the magnitude of valley-orbit slitting

Stress along the <111> direction does not affect the degeneracy of the conduction band minima and so the magnitude of the valley-orbit splitting (recall from Sec.1.3 that this splitting is due to the six-fold degeneracy of the conduction band) will not be affected either.

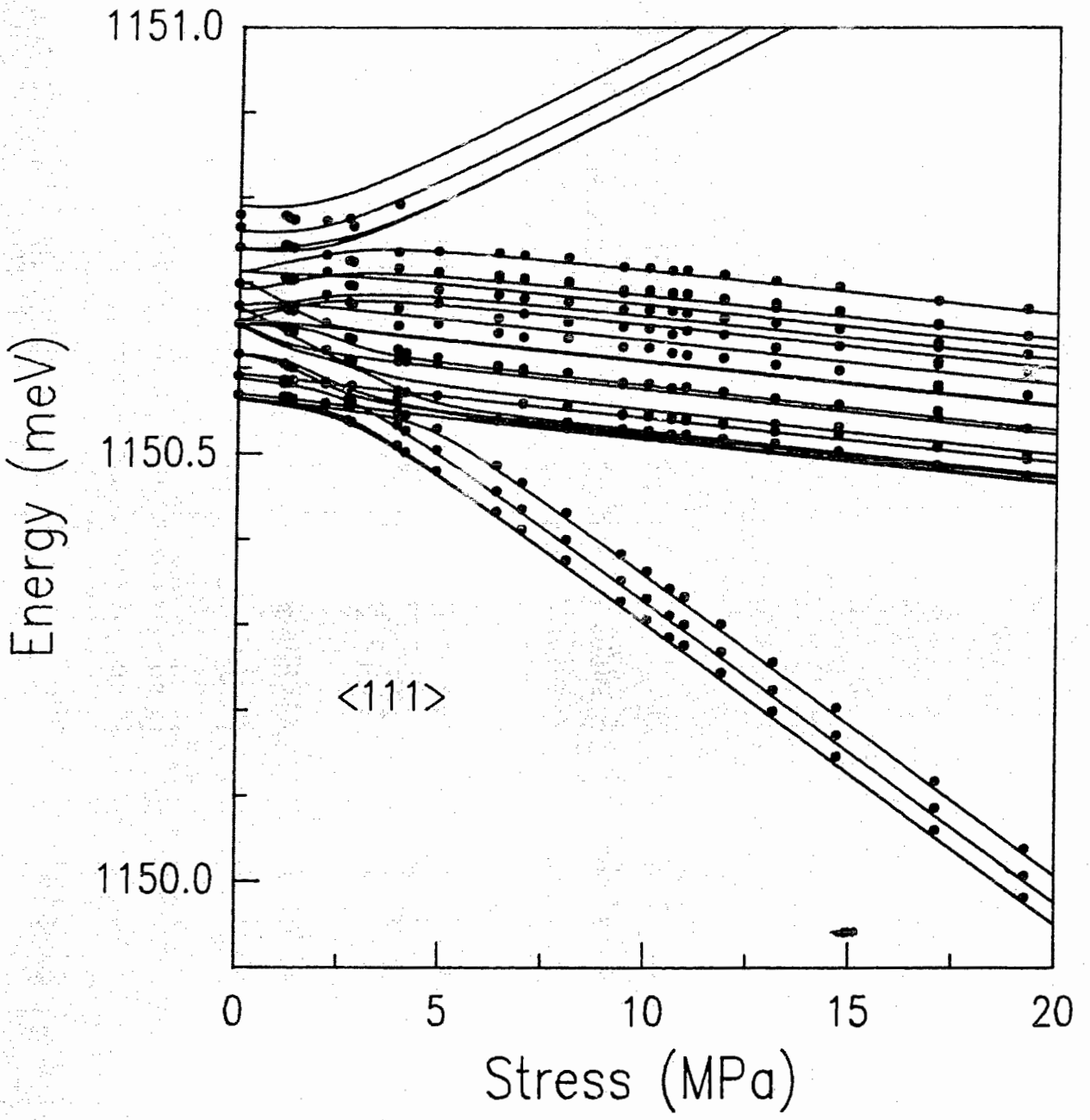

Fig. 4.5 Energy of the boron bound exciton energy levels as a function of stress along the <111> direction. The lines represent the predicted energy levels and will be discussed in Sec. 4.4.

On the other hand, any uniaxial stress splits the two fold degenerate hole shell into two subshells. At high stress, when the splitting associated with the single hole states is large compared to the zero stress splitting of the bound exciton levels, both holes in the bound exciton occupy the lower energy hole state. In this case, the antisymmetrized product of the two hole states transforms as Γ_1. There will thus be no splitting due to the hole-hole interaction and in addition the two holes will not interact with the electron (for a more thorough explanation see refs [92K1] and [83K]).

Hence, at high stress, the contribution of electron-hole and hole-hole interactions to the splitting of the bound exciton energy levels is negligible and the only contribution to the splitting of the bound exciton energy levels is from valley-orbit splitting. The magnitude of the valley-orbit splittings can be obtained directly from the bound exciton luminescence spectrum under high stress along the <111> direction.

Fig. 4.6 shows the bound exciton luminescence when a stress of 24 MPa is applied along the <111> direction, plus a sketch of a transition scheme which would produce this spectrum.. The three spectral components, labelled a, b, and c thus correspond to transitions from the three levels of the bound exciton, labelled Γ_3, Γ_5 and Γ_1 (this particular ordering of levels was determined elsewhere [92K2]), to the lower level of the neutral acceptor (since the holes in the bound exciton are in the lower energy states, only transitions to the lower hole state of the neutral acceptor are observed). The splitting between components in the spectrum directly reflects the spacing of the bound

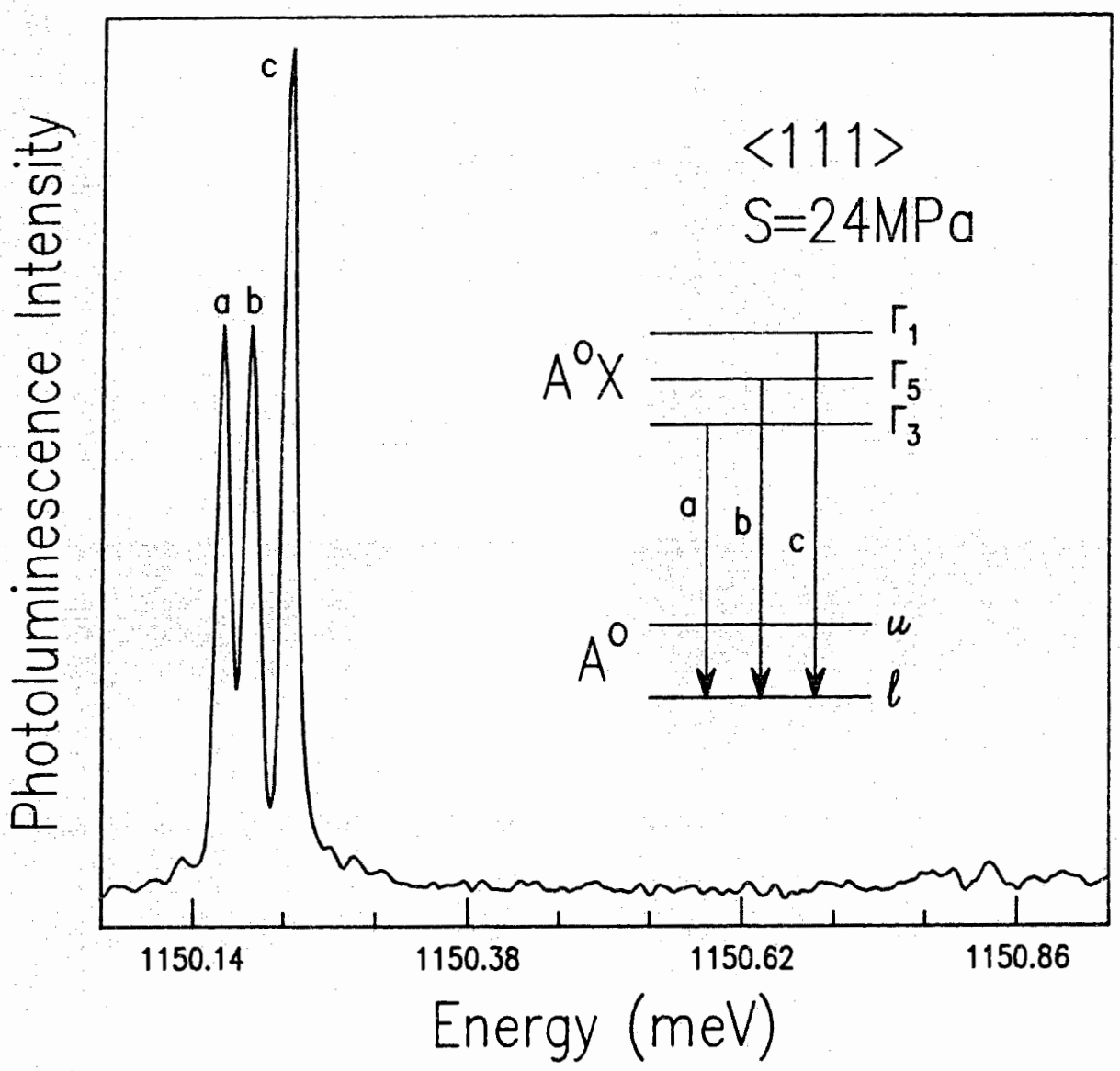

Fig. 4.6 Boron bound exciton luminescence when a stress of 24 MPa is applied along the <111> direction. The inset shows the boron bound exciton to neutral acceptor transition scheme for high stress along the <111> direction.

exciton energy levels and thus the magnitude of the valley orbit splitting. By measuring the splitting between components c and a, and b and c, the valley orbit splitting constants are thus assigned the values Δ_1 = 32 μeV and Δ_3 = -26 μeV, where Δ_1 is the energy difference between the Γ_1 and Γ_3 levels and Δ_3 is the energy difference between the Γ_3 and Γ_5 levels.

4.3.3 High stress along <001> and <110>

It was important to go to high stress (24 MPa) along the <111> direction since the goal was to obtain the valley-orbit splitting parameters. When the data was collected along the other two directions, the maximum stress applied was lower, since data at higher stress was not necessary for an energy level diagram and no further quantitative information could be gained by going to higher stress. However, the evolution of the luminescence with stress can be extrapolated to give a picture of the high stress behavior.

As stress is applied, the bound exciton energy levels move farther apart, with some moving up in energy and some moving down. As this happens, the population of the levels which move to higher energy will decrease, the consequence being an increase in the population of levels at lower energy. Transitions from levels which move up in energy will thus disappear with increasing stress and are said to "thermalize". As the temperature in decreased, the population of the lower levels will increase even more and the higher energy states will become virtually "empty". Fig.4.7 shows the luminescence when 11 MPa of stress are

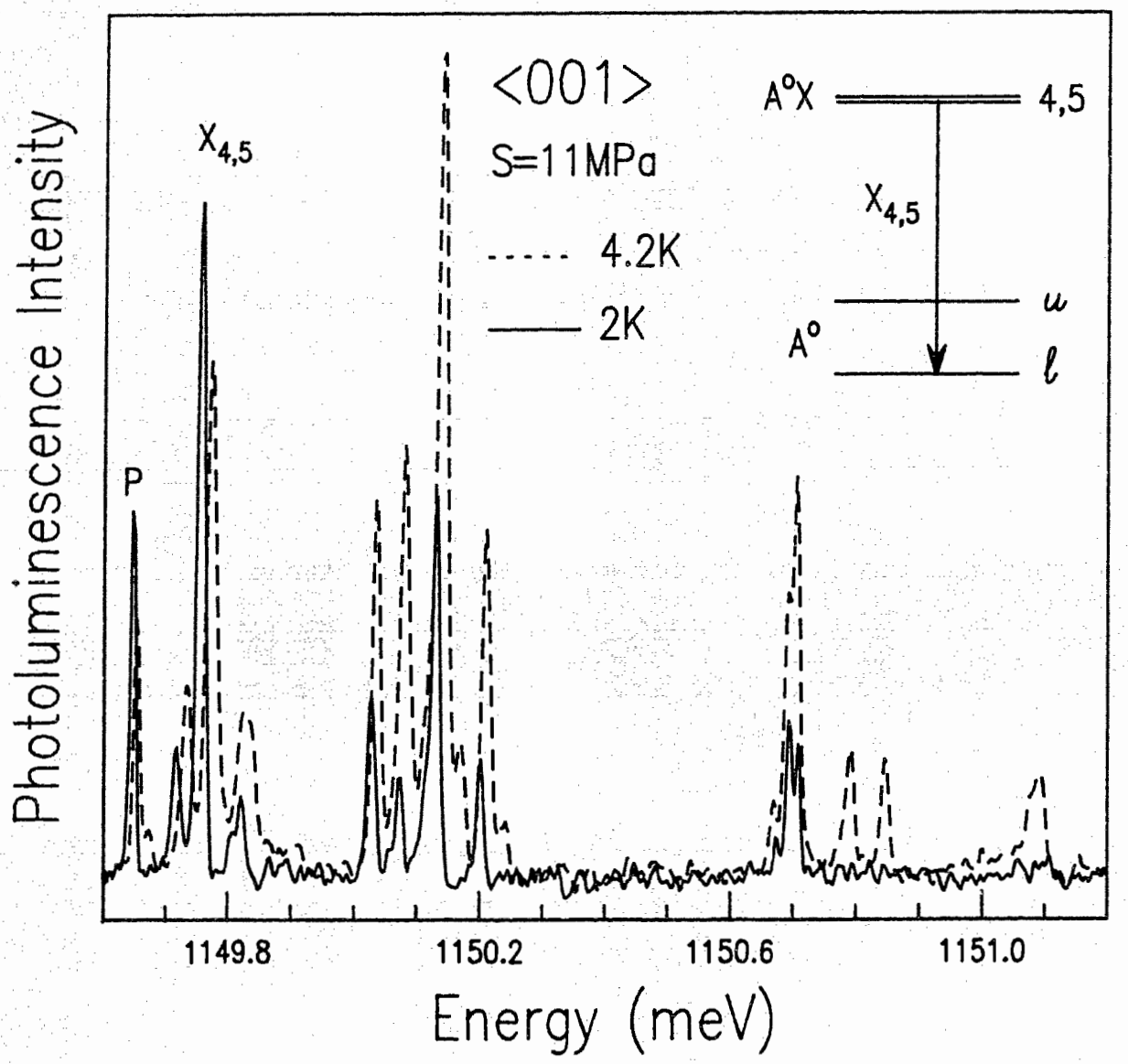

Fig. 4.7 Boron bound exciton luminescence when a stress of 11 MPa is applied along the <001> direction. The inset shows the boron bound exciton to neutral acceptor transition scheme for high stress along a <001> direction.

applied along the <001> direction (the transition scheme shown on the right will be explained later). The dotted curve is the spectrum taken at 4.2 K and the solid curve is the spectrum at 2 K. When the temperature is decreased, the intensity of component $X_{4,5}$ increases while the intensity of all other components decreases, implying that component $X_{4,5}$ is a transition from the lowest energy state.

Fig. 4.8 shows the bound exciton luminescence at three different stresses along the <001>. Note that the intensity of component $X_{4,5}$ increases relative to the other components as the stress increases. This combined with the increase in intensity of component $X_{4,5}$ as the temperature decrease, leads to the conclusion that as stress increases further, component $X_{4,5}$ will be the only non-thermalizing component in the spectrum, i.e., only one energy level will be populated in the limit of high stress along <001>.

The behavior of the luminescence under high <110> stress is more straightforward. Fig. 4.9 shows the bound exciton luminescence at three different stresses along <110>. Fig. 4.10 shows the luminescence at 18 MPa, the highest stress applied along this direction (again, the transition scheme will be explained later). From Fig. 4.9, it is seen that as stress increases, the intensities of components (1,2) and (3) increase relative to the other components. In Fig. 4.9, these components emerge as the main features and we can infer that as stress increases further they will be the only remaining components, i.e. two energy levels will be populated at liquid helium temperature, in the limit of high stress along <110>.

As was discussed above, the splitting of energy levels at high

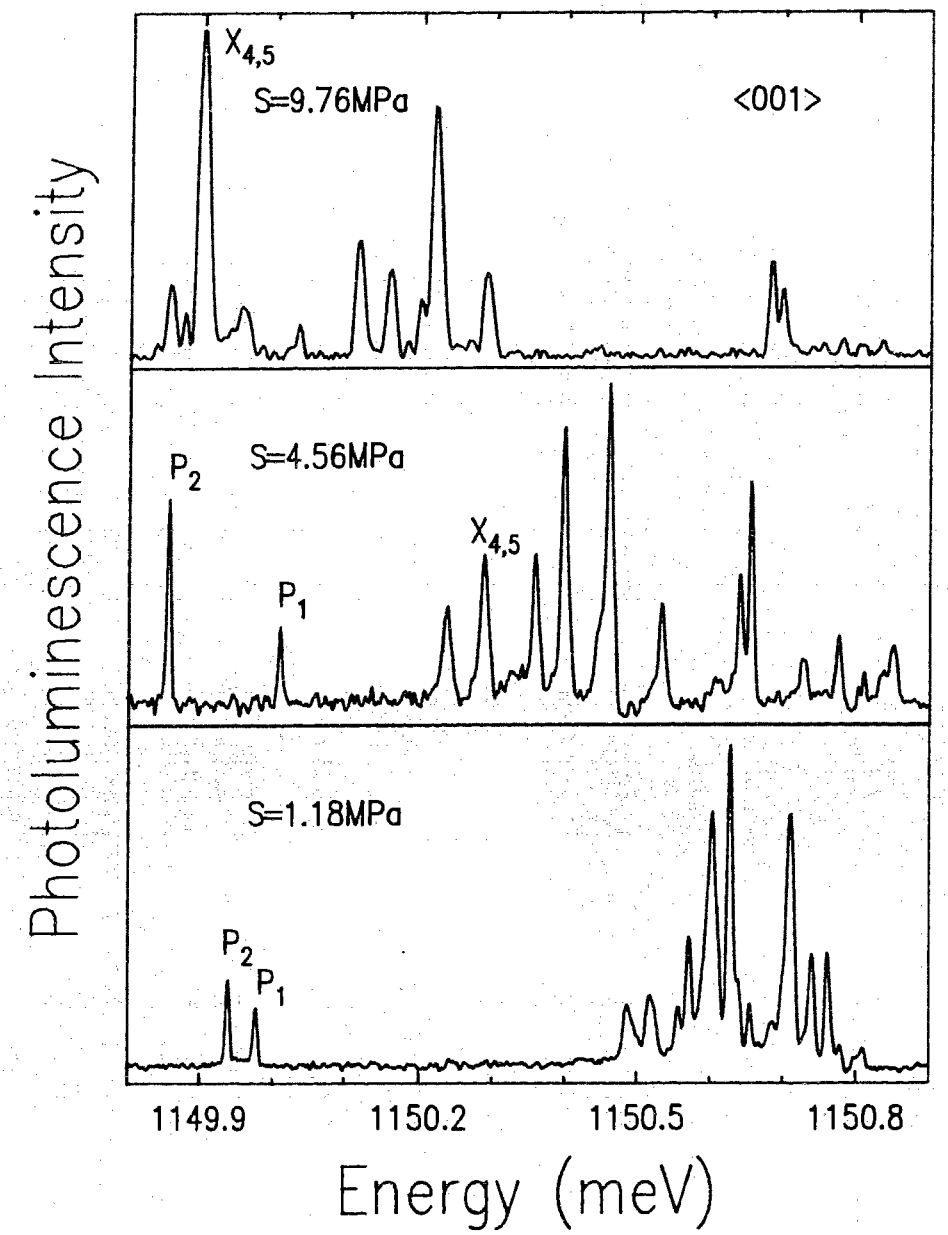

Fig. 4.8 Boron bound exciton luminescence when three different stresses are applied along the <001> direction. The lines P_1 and P_2 are due to the phosphorous bound exciton.

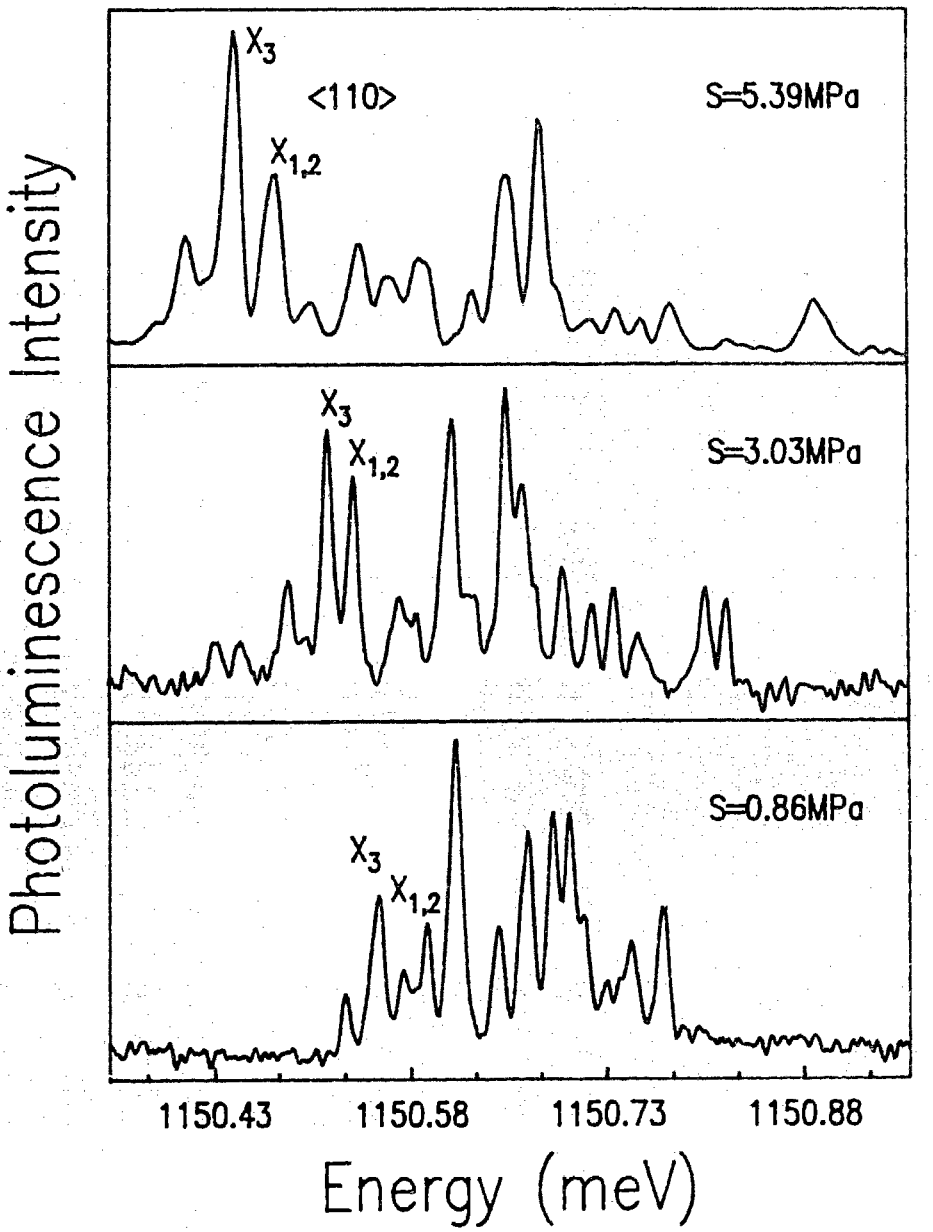

Fig. 4.9 Boron bound exciton luminescence when three different stresses are applied along the <110> direction.

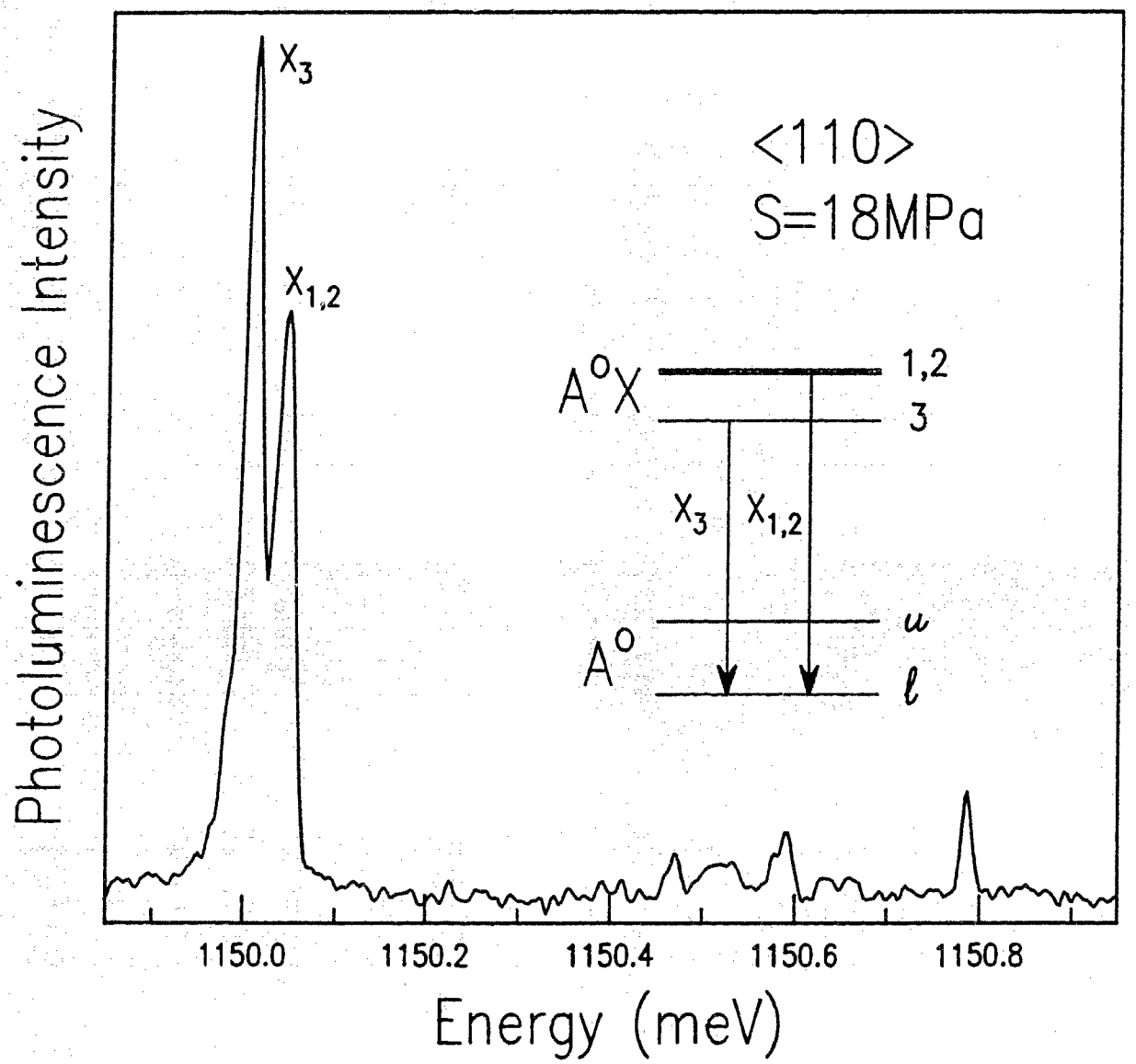

Fig. 4.10 Boron bound exciton luminescence when a stress of 18 MPa is applied along the <110> direction. The inset shows the boron bound exciton to neutral acceptor transition scheme for high stress along the <110> direction.

stress will be dominated by the splitting of the electron states. Thus by looking at the behavior of the electron states under stress, the bound exciton luminescence spectrum at high stress along <001> and <110> can be predicted and compared with the observed spectra.

Recall that at zero stress the single electron states transform according to the irreducible representations Γ_1, Γ_3, and Γ_5 which are, respectively, one-, two- and three-fold degenerate (not counting spin). This splitting of the originally six-fold degenerate electron energy level arose when the reduction of symmetry ($O_h \rightarrow T_d$) due to the introduction of an impurity into the crystal was taken into account (see Sec. 1.3). When uniaxial stress is applied, the crystal symmetry is further reduced ($T_d \rightarrow C_{3v}$, $T_d \rightarrow C_{2v}$, and $T_d \rightarrow D_{2d}$ for stress along <111>, <110>, and <001> respectively) and the electron energy levels will split again. The energies of the single electron levels as a function of stress along <001> and <110> [92K1] are presented in Fig. 4.11. The energy associated with the Γ_1 state will be unsplit and will increase for stress along both <001> and <110>. For both directions, the Γ_5 energy level will split into two with one level going up in energy and one going down. The Γ_3 energy level will also split into two levels, but for stress along <001> one level will go up in energy and one will go down, while for stress along <110> both levels will go down in energy (although one split Γ_3 level originally goes up before dropping down).

Only those levels which go down in energy as a function of stress will be populated at low temperature. Thus for high stress along <110> three energy levels should be populated and for high stress along <001> two levels should be populated. The transitions from these bound

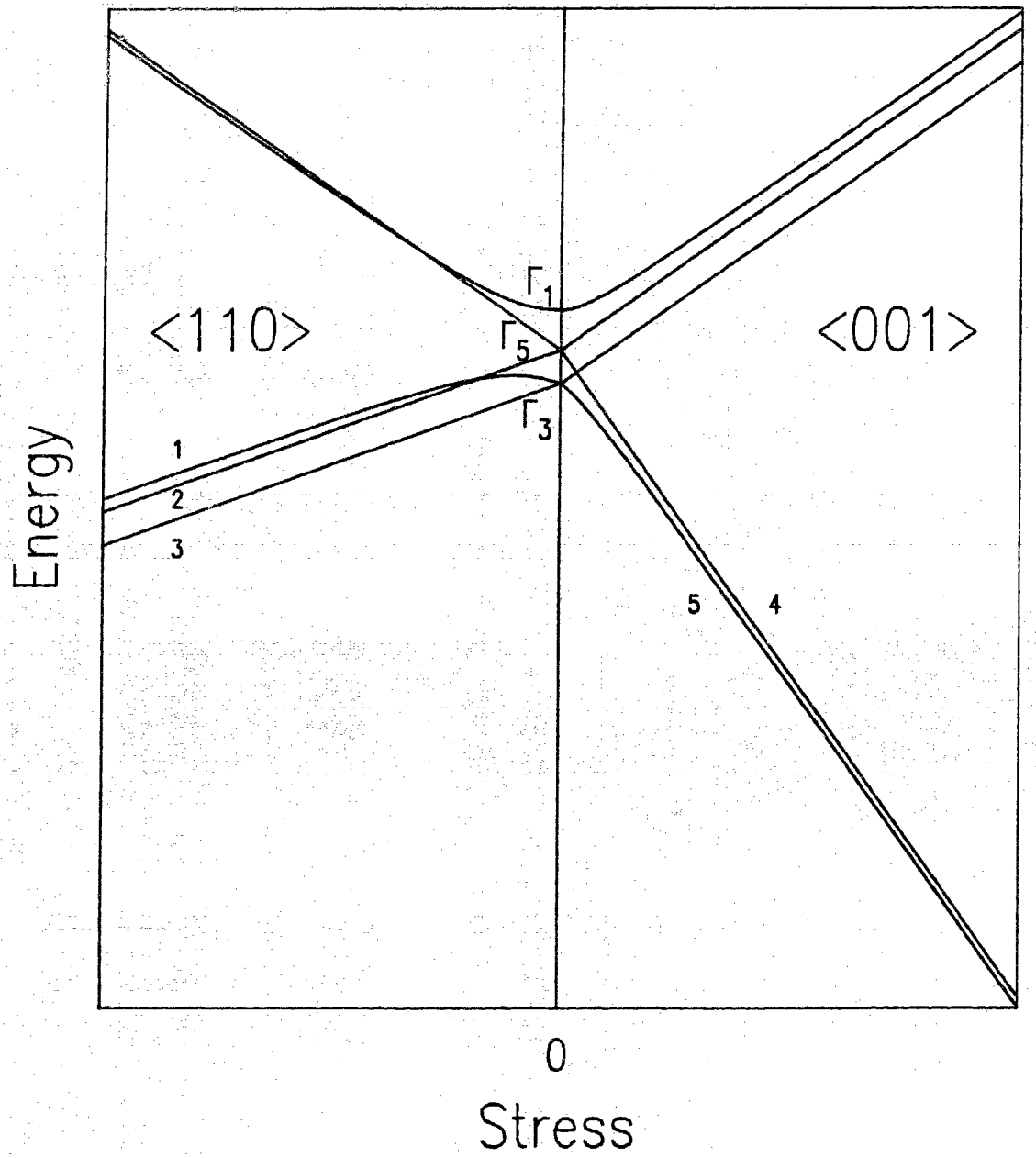

Fig. 4.11 Splitting of the energy levels associated with the single electron valley-orbit states as a function of stress along the <110> and <001> directions.

exciton levels to the neutral acceptor (again, transitions will be to the lower neutral acceptor level) are presented for the <110> direction in Fig.4.10 and the <001> direction in Fig.4.7. These transition schemes show three possible transitions for <110> and two for <001>. However, since the energy difference between levels 1 and 2, and between 4 and 5 is smaller than our available resolution transitions from these states should be unresolved in the spectra. Thus the predicted spectrum for high <110> stress would consist of two components while the similar spectrum for <001> would have only one component. This agrees with the experimental results discussed above.

4.4 CONCLUSION

High resolution no-phonon photoluminescence spectra of the boron bound exciton under uniaxial stress have been presented. These spectra consist of up to thirty very narrow lines (less than 10 μeV FWHM) and reflect the complicated interactions responsible for the zero-stress fine structure of the boron bound exciton (nine well resolved lines).

These results have been used to test the newly formulated theory of the acceptor bound exciton [92K1]. As mentioned in Sec.1.6, the energy eigenvalues of the perturbation Hamiltonian

$$H = H_{vo} + H_{es} + H_{hs} + H_{hh} + H_{eh}. \qquad \text{eqn.(1.12)}$$

yield the position of the exciton energy levels. The term H_{vo} contains

the valley orbit parameters which were determined from the <111> spectra at high stress (Sec. 4.3.2). The remaining parameters are obtained by a best-fit comparison of the predicted energies to those observed - the lines in Fig. 4.5 represent the predicted energy levels as a function of stress along <111>.

Fig. 4.12 shows the zero stress bound exciton spectrum plus tickmarks which indicate the predicted positions of the fine structure lines. The tickmarks on the low-energy end line up well with the observed features, but the last tickmark at ~1150.78 meV does not. This model gives a convincing fit, but clearly it can be improved upon. One way of improving things is to model the bound exciton energy levels as a function of both uniaxial stress and magnetic field. As is the case with stress, by applying a magnetic field, conduction and valence band degeneracies are removed in a predictable way and the resulting perturbation Hamiltonian (which includes many of the same interaction parameters) can be formulated. By simultaneously best-fitting both sets of data, a better estimate of the parameters can be made and thus more accurate predictions of spectral positions can be given.

We have obtained the first high-resolution spectra of the boron bound exciton under stress. These results allow theoretical modeling of the acceptor bound exciton, such as discussed in the previous paragraph, to proceed. In addition, we have determined for the first time the values of the valley-orbit interaction constants for the boron acceptor. The ability to obtain the results presented here was due almost entirely to the powerful spectroscopic technique used and the uniformity of the applied uniaxial stress.

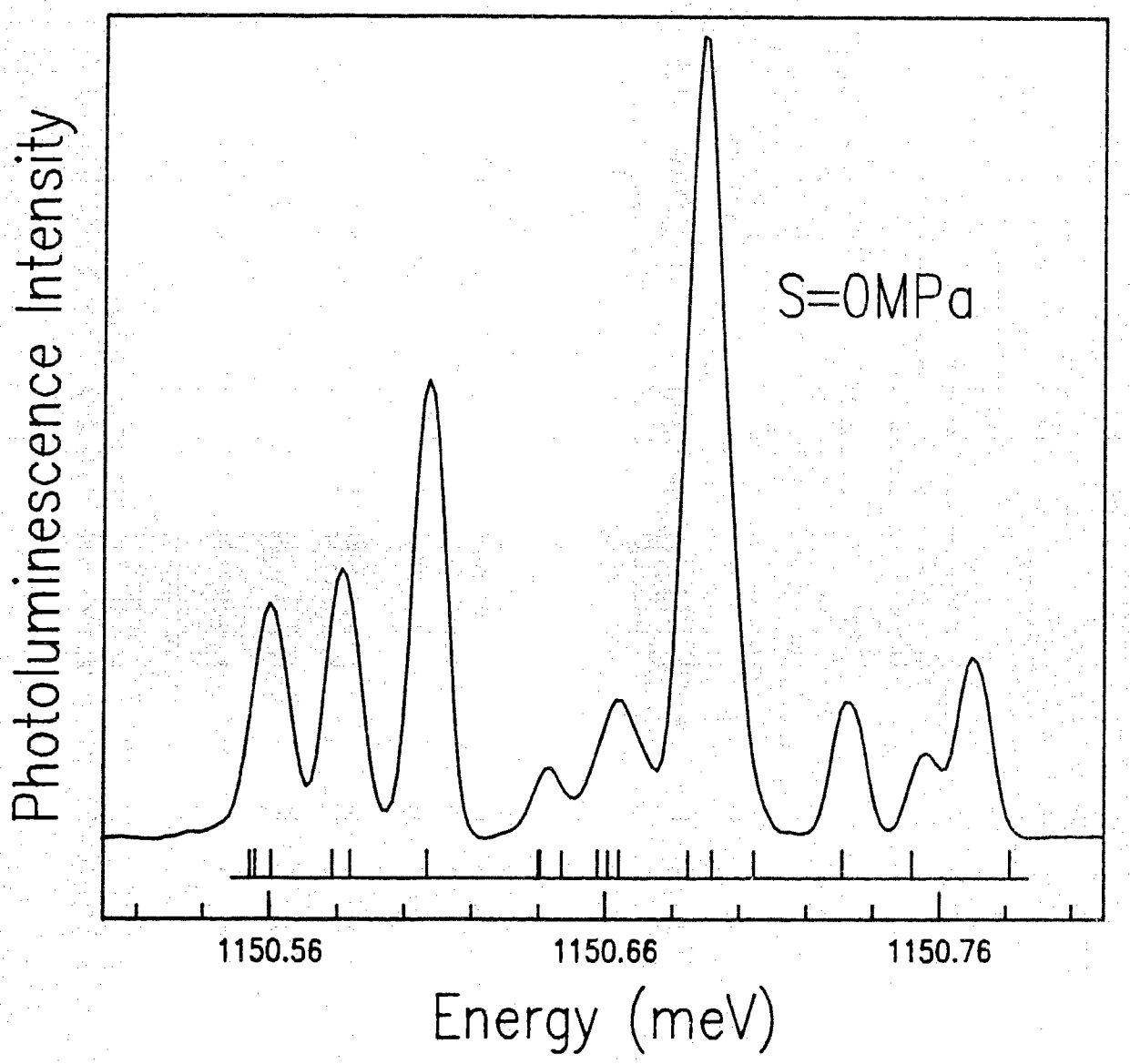

Fig. 4.12 Boron bound exciton luminescence at zero stress. The tickmarks indicate the spectral positions predicted by the model described in ref. [92K1]

REFERENCES

55K W. Kohn and J.M. Luttinger, Phys. Rev. **98**, 915 (1955).

57K W. Kohn, in *Solid State Physics*, Vol.5, edited by H. Ehrenreich, Academic Press Inc., New York (1957).

58L M.A. Lampert, Phys. Rev. Lett. **1**, 450 (1958).

60H J.R. Haynes, Phys. Rev. Lett. **4**, 361 (1960).

63K K. Nishikawa and R. Barrie, Can. J. Phys. **41**, 1135 (1963).

67D P.J. Dean, W.F. Flood, and G. Kaminskii, Phys. Rev. **163**, 721 (1967).

70K1 A.S. Kaminskii and Ya.E. Pokrovskii, JETP Lett. **11**, 255 (1970).

70K2 A.S. Kaminskii and Ya.E. Pokrovskii N.V. Alkeev, Sov. Phys. JETP. **32**, 1048, (1971).

70P Ya.E. Pokrovskii, A.S. Kaminskii, K. Svistunova, *Procedings of the Tenth International Conference on the Physics of Semiconductors*, edited by S.P. Keller, J.C. Hensel, and F. Stern, USAEC, Springfield, VA, p.504. (1970)

73S R. Sauer, Phys. Rev. Lett. **31**, 376 (1973).

73W A.M. White, A.M. J. Phys. C. **6**, 1971 (1973).

74K K. Kosai and M. Gershenzon, Phys. Rev. B **9**, 723 (1974).

75B F. Bassani and Pastori Parravicini, *Electronic States and optical Transitions in Solids*, Pergamon Press Inc., Great Britain (1975).

76A N.W. Ashcroft and N.D. Mermin, *Solid State Physics*, Holt, Rinehart, and Winston, Inc., Philadelphia, (1976).

76D P.J. Dean, D.C. Herbert, D. Bimberg and W.J. Choyke, Phys. Rev. Lett. **37**, 1635 (1976).

76M T.N. Morgan, *Proceedings of Thirteenth International Conference on the Physics of Semiconductors*, Rome, p.825 (1976).

76S R. Sauer and J. Weber. Phys. Rev. Lett **36**, 48 (1976).

76V M.A. Vouk and E.C. Lightowlers, *Proceedings of Thirteenth International Conference on the Physics of Semiconductors*, Rome, p.1098 (1976).

77K G. Kirczenow, Can. J. Phys. **55**, 1787 (1977).

77L E.C. Lightowlers and M.O. Henry, J. Phys. C **10**, L247 (1977).

77M T.N. Morgan, J. Phys. C **10**, 1131, (1977)

77R T.M. Rice in *Solid State Physics*, Vol.32, edited by H. Ehrenreich, F. Seitz, and D. Turnbull, Academic Press Inc., New York (1977).

77T1 M.L.W. Thewalt, Can. J. Phys. **55**, 1463 (1977).

77T2 M.L.W. Thewalt, Phys Rev. Lett. **38**, 521 (1977).

78E1 K.R. Elliott, G.C. Osbourn, D.L. Smith, and T.C. McGill, Phys. Rev. B **17**, 1808 (1978).

78E2 K.R. Elliott and T.C. McGill, Solid State Comm. **28**, 491 (1978).

78E3 K.R. Elliott, D.L. Smith and T.C. McGill, Solid State Comm. **27**, 317 (1978).

78K A.S. Kaminskii, V.A. Karasyuk, and Ya.E. Pokrovskii, Sov. Phys. JETP **47** (6) (1978).

78T M.L.W. Thewalt and J.A. Rostworowski, Phys. Rev. Lett. **41**, 808 (1978).

79T M.L.W. Thewalt, J.A. Rostworowski, and G. Kirczenow, Can. J. Phys. **57**, 1898 (1979).

81K1 C. Kittel, *Introduction to Solid State Physics*, 6th ed., Wiley, New York (1981).

81K2 A.S. Kaminskii, V.A. Karasyuk, Ya.E. Pokrovskii, JETP Lett. 33, 133 (1981).

81L M. Lannoo and J. Bourgin, *Point Defects in Semiconductors I, Theoretical Aspects*, Springer Series in Solid State Sciences, Vol.20, Springer-Verlag, Berlin, (1981).

81R A.K. Ramdas and S. Rodriguez, Reports on Progress in Physics **44**, 1297 (1981).

82S K. Seeger, *Semiconductor Physics, An Introduction*, Springer Series in Solid State Sciences, Vol.40, Springer-Verlag, Berlin, (1982).

82T M.L.W. Thewalt, in *Excitons*, edited by E.I. Rashba and M.D. Sturge, North Holland, New York (1982).

83K V.A. Karasyuk and Ya.E. Pokrovskii, JETP Lett. **37**, 11 (1983).

86G P.R. Griffiths and J.A. de Haseth, *Fourier Transform Infrared Spectroscopy*, John Wiley and Sons, New York (1986).

88G M.V. Gorbunov, A.S. Kaminskii, and A.N. Saffonov, Sov. Phys. JETP **67** (2) 355 (1988).

89L Landolt-Börnstein, *Numerical Data and Functional Relationships in Science and Technology, New Series,* group III, vol.22, Semiconductors, subvolume b, editor in chief O. Madelung, Springer-Verlag, Berlin (1989).

90K V.A. Karasyuk, E.C. Lightowlers, M.L.W. Thewalt, A.G. Steele, and D.M. Brake, Mat Sci.Forum, Vols 65-66, p.205 (1990).

90T M.L.W. Thewalt, M.K. Nissen, D.J.S. Beckett, and K.R. Lundgren, Mat. Res. Soc. Symp. Proc., Vol.163 (1990).

91C E.R. Cohen and B.N. Taylor, Physics Today, Part 2: Buyers'Guide, p.BG9, August (1991).

92K1 V.A. Karasyuk, A.G. Steele, A. Mainwood, E.C. Lightowlers, D.M. Brake, and M.L.W. Thewalt, Phys. Rev. B **45**, 736 (1992).

92K2 V.A. Karasyuk, D.M. Brake, and M.L.W. Thewalt, submitted for publication to Phys. Rev. B, (1992).